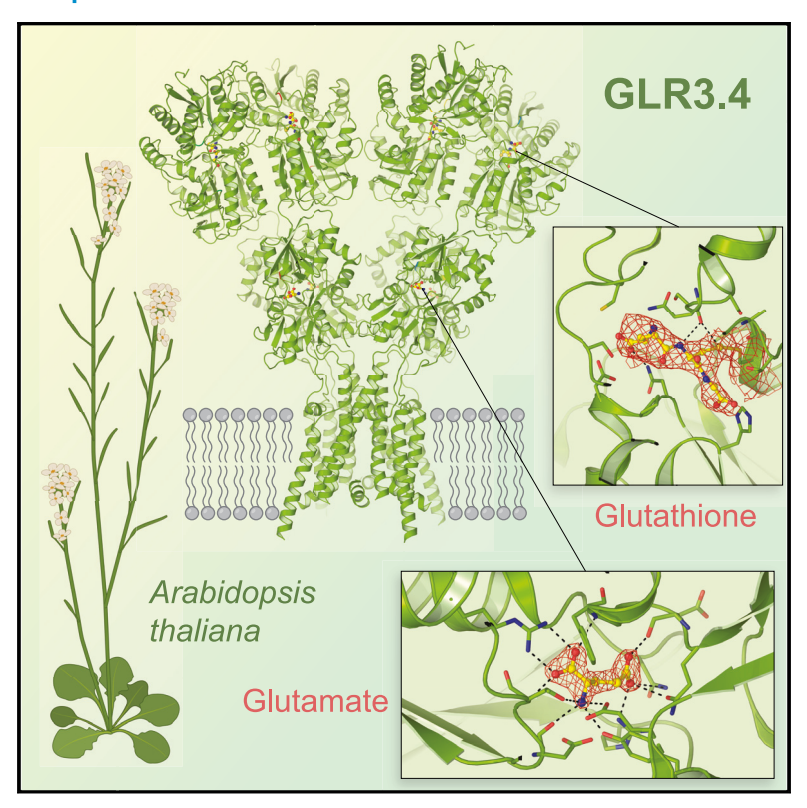
# Structure of the *Arabidopsis thaliana* glutamate receptor-like channel GLR3.4

### **Graphical abstract**



### **Highlights**

- Cryo-EM structure of Arabidopsis thaliana glutamate receptor-like channel GLR3.4
- Glutathione regulates channel activity by binding to C205 in amino-terminal domain
- Crystal structures of GLR3.4 ligand-binding domain illustrate ligand promiscuity
- Amino-terminal and ligand-binding domain layers show nonswapped domain arrangement

### **Authors**

Marriah N. Green, Shanti Pal Gangwar, Erwan Michard, ..., Maria V. Yelshanskaya, José A. Feijó, Alexander I. Sobolevsky

### Correspondence

as4005@cumc.columbia.edu

### In brief

Green et al. solve structures of Arabidopsis thaliana glutamate receptorlike channel GLR3.4 that shows tetrameric subunit assembly with threelayer architecture, similar to its mammalian homologs, ionotropic glutamate receptors, but with distinct symmetry, inter-domain interfaces, ligand specificity, and non-swapped domain arrangement between layers of ligand-binding and glutathione-bound amino-terminal domains.





### **Article**

### Structure of the *Arabidopsis thaliana* glutamate receptor-like channel GLR3.4

Marriah N. Green. 1,2,6 Shanti Pal Gangwar, 1,6 Erwan Michard, 3,4,7 Alexander A. Simon, 3,7 Maria Teresa Portes, 3,8 Juan Barbosa-Caro, Michael M. Wudick, 3,5 Michael A. Lizzio, Oleg Klykov, Maria V. Yelshanskaya, José A. Feijó, 3 and Alexander I. Sobolevsky1,9,\*

<sup>1</sup>Department of Biochemistry and Molecular Biophysics, Columbia University, 650 West 168th Street, New York, NY 10032, USA

<sup>2</sup>Training Program in Nutritional and Metabolic Biology, Institute of Human Nutrition, Columbia University Irving Medical Center, 630 West 168th Street, New York, NY 10032, USA

<sup>3</sup>University of Maryland, Department of Cell Biology and Molecular Genetics, 0118 BioScience Research Building, College Park, MD

<sup>4</sup>Instituto de Ciencias Biológicas, 2 Norte 685, Universidad de Talca, 3460000 Talca, Chile

<sup>5</sup>Institute for Molecular Physiology, Heinrich Heine Universität, Universitätsstrasse 1, 40225 Düsseldorf, Germany

<sup>6</sup>These authors contributed equally

<sup>7</sup>These authors contributed equally

<sup>8</sup>Current address: Departamento de Botânica, Instituto de Biociências, Universidade de São Paulo, 05508-090, São Paulo, Brazil

<sup>9</sup>Lead contact

\*Correspondence: as4005@cumc.columbia.edu https://doi.org/10.1016/j.molcel.2021.05.025

### **SUMMARY**

Glutamate receptor-like channels (GLRs) play vital roles in various physiological processes in plants, such as wound response, stomatal aperture control, seed germination, root development, innate immune response, pollen tube growth, and morphogenesis. Despite the importance of GLRs, knowledge about their molecular organization is limited. Here we use X-ray crystallography and single-particle cryo-EM to solve structures of the Arabidopsis thaliana GLR3.4. Our structures reveal the tetrameric assembly of GLR3.4 subunits into a three-layer domain architecture, reminiscent of animal ionotropic glutamate receptors (iGluRs). However, the non-swapped arrangement between layers of GLR3.4 domains, binding of glutathione through S-glutathionylation of cysteine C205 inside the amino-terminal domain clamshell, unique symmetry, inter-domain interfaces, and ligand specificity distinguish GLR3.4 from representatives of the iGluR family and suggest distinct features of the GLR gating mechanism. Our work elaborates on the principles of GLR architecture and symmetry and provides a molecular template for deciphering GLR-dependent signaling mechanisms in plants.

### **INTRODUCTION**

Glutamate receptor-like channels (GLRs) have been identified as homologs of mammalian ionotropic glutamate receptors (iGluRs), which mediate the majority of the excitatory neurotransmission in the central nervous system (Traynelis et al., 2010). GLR homologs have been identified in both vascular and non-vascular plants (Lam et al., 1998; Wudick et al., 2018a) and in genomes across the entire plant evolutionary tree, including Chlamydomonas, chlorophytes, mosses, ferns, gymnosperms, and angiosperms (De Bortoli et al., 2016; Wudick et al., 2018a). On the basis of phylogenetic analysis, the 20 GLRs identified in the model flowering plant Arabidopsis thaliana have been organized into three different clades: GLR1, GLR2, and GLR3 (Lam et al., 1998). In contrast to iGluRs, which are targeted mainly to the plasma membrane, GLRs have not only been located in the plasma membrane but also located in the plant mitochondria, chloroplast, tonoplast, endoplasmic reticulum, and sperm cell (endo)membranes (Teardo et al.,

2015; Vincill et al., 2013; Wudick et al., 2018a). GLRs play vital roles in various physiological processes in plants, such as cell signaling, metabolism, wound response, stomatal aperture, seed germination, root development, innate immune response, pollen tube growth, and water loss (Wudick et al., 2018a). Given the diverse range of crucial physiological roles, targeting GLRs can have practical applications, especially related to biotic and abiotic environmental stress, which constitute a major problem for sustainability (Jones et al., 2008). Genetic efforts to explore GLR potential have been hindered by the apparent high functional redundancy and a large number of genes coding for GLRs in the majority of angiosperms, including crops. An alternative to traditional strategies for regulating GLR functions in plants could use approaches that target their specific molecular features (De Bortoli et al., 2016; Michard et al., 2017; Wudick et al., 2018a, 2018b).

The molecularly oriented approaches to harness GLR function rely on the detailed knowledge of GLR structural organization. Recent studies of the GLR3.2 and GLR3.3 ligand-binding

### **CellPress**

### **Molecular Cell Article**

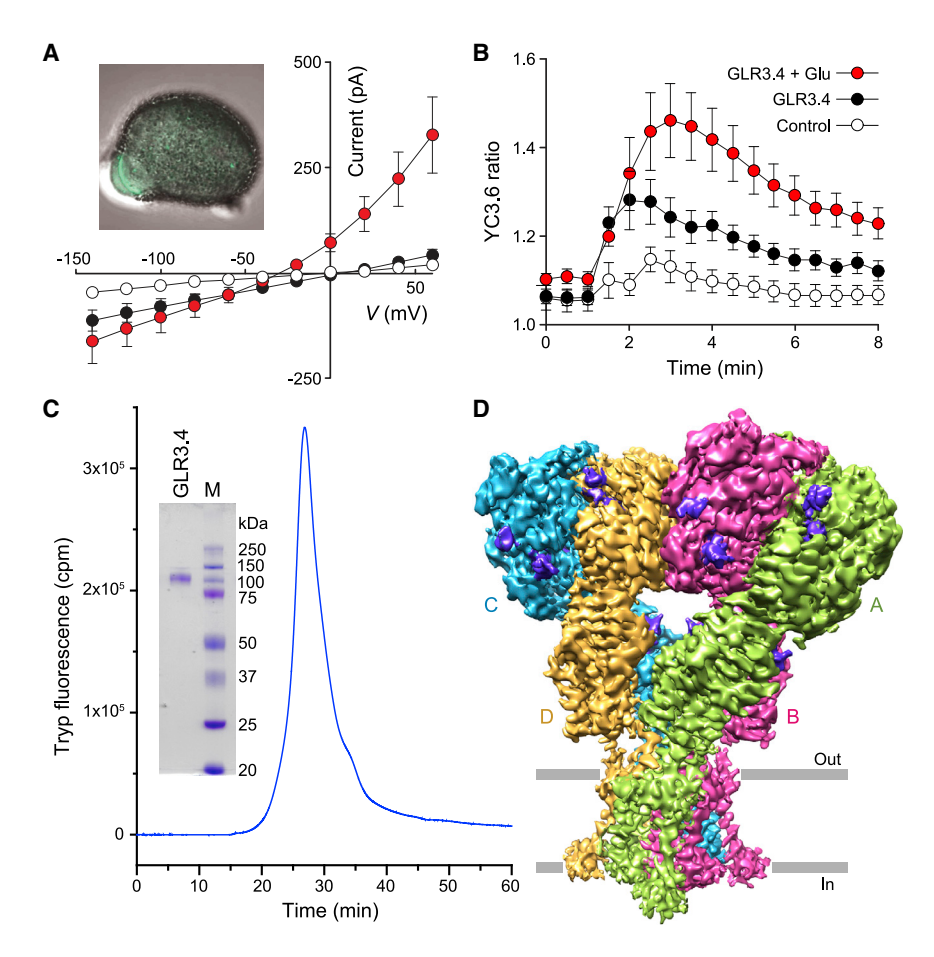


Figure 1. Functional, biochemical, structural characterization of GLR3.4

(A) Voltage dependence of whole-cell patchclamp currents recorded from COS-7 cells expressing GLR3.4, CNIH1, and CNIH4 before (black circles) and after (red circles) application of 1 mM Glu (n = 3, mean  $\pm$  SEM). The control (white circles) is endogenous currents recorded from COS-7 cells transfected with the empty vector (n = 5, mean ± SEM). Inset shows specific GFP labeling of GLR3.4 at the plasma membrane of the pollen grain aperture, an outgrowth spot where the pollen tube will emerge.

(B) Changes in cytosolic Ca2+ measured in COS-7 cells expressing the Ca2+ sensor Yellow CaMeleon 3.6 (YC3.6) and expressing either CNIH1+4 alone (control, white circles) or GLR3.4 and CNIH1+4, in response to application of 14.5 mM Ca2+ in the absence (black circles; n = 27, mean ± SEM) or presence (red circles; n = 33, mean ± SEM) of 1 mM Glu.

(C) FSEC trace and SDS-PAGE gel for purified GLR3.4.

(D) Cryo-EM density for 3.57 Å 3D reconstruction of GLR3.4, with four subunits colored in green, pink, blue, and orange, and non-protein densities representing carbohydrates and ligands colored in purple.

See also Figures S1-S3 and Table S1.

localizes specifically to the aperture of the pollen grain (Figure 1A) and appears to be associated with cell polarity, from the formation of the early bulge, which will develop into the pollen tube, to the reten-

tion in the apical tips after the formation of the callose plugs, or in root phloem cells (Vincill et al., 2013; Figures S1A-S1C). Cell polarity in *Arabidopsis* pollen tubes has also been characterized by the tip-focused influx of calcium (Ca2+) (Michard et al., 2011, 2017). Supporting the role of GLR3.4 in this cell polarity process, two mutant alleles of glr3.4 showed reduced pollen tube Ca2+ fluxes compared with wild-type (Figure S1D).

GLR3.4 was reported to mediate currents activated by a broad range of amino acids (Meyerhoff et al., 2005; Stephens et al., 2008; Vincill et al., 2012). GLR3.4 expressing COS-7 cells showed robust ionic currents in response to application of Glu or Asn only when co-expressed with CORNICHON HOMOLOG (CNIH) proteins CNIH1 and/or CNIH4 (Figure 1A; Figures S2A-S2D), consistent with the recently discovered role of CNIHs in GLR sorting and activation (Wudick et al., 2018b). GLR3.4 activation in the presence of Glu or Asn resulted in an increase in cytosolic calcium (Figure 1B; Figures S2E and S2F), which may work as a signaling mechanism in plants (Michard et al., 2011; Mousavi et al., 2013; Ortiz-Ramírez et al., 2017).

We expressed full-length GLR3.4 in HEK293 cells, purified the protein to sufficient purity and homogeneity (Figure 1C), and subjected it to single-particle cryoelectron microscopy (cryo-EM). We reconstructed a three-dimensional (3D) map to an overall 3.57 Å resolution (Figure 1D), with the core of the molecule resolved at ~3 Å resolution (Figure S3; Table S1; Video S1).

domains (LBDs), from the model organism Arabidopsis thaliana, provided the first glimpse of the fragment of GLR structure responsible for ligand binding (Alfieri et al., 2020; Gangwar et al., 2021). GLR3.2 and GLR3.3 LBD structures identified similar overall folds to iGluRs' LBD structures, with the distinct features in the ligand-binding pocket that are responsible for the promiscuous GLR activation by various amino acids. Despite the important insights from the recent structural studies of GLR LBDs, structures of other GLR domains, principles of their assembly into the full-length receptor, its architecture, and the structural basis of gating have remained an enigma. To fill this gap in knowledge, we embarked on the endeavor to determine the structure of a full-length GLR.

### **RESULTS**

### **Functional characterization and structure** determination

We screened several full-length GLRs from the three different clades using fluorescence-detection size-exclusion chromatography (FSEC) (Kawate and Gouaux, 2006) and identified GLR3.4 from Arabidopsis thaliana as a promising candidate for structural studies. GLR3.4 expresses at the plasma membrane of root phloem cells, vascular bundles, mesophyll cells, and guard cells (Meyerhoff et al., 2005; Vincill et al., 2013). We show that GLR3.4

**Article** 



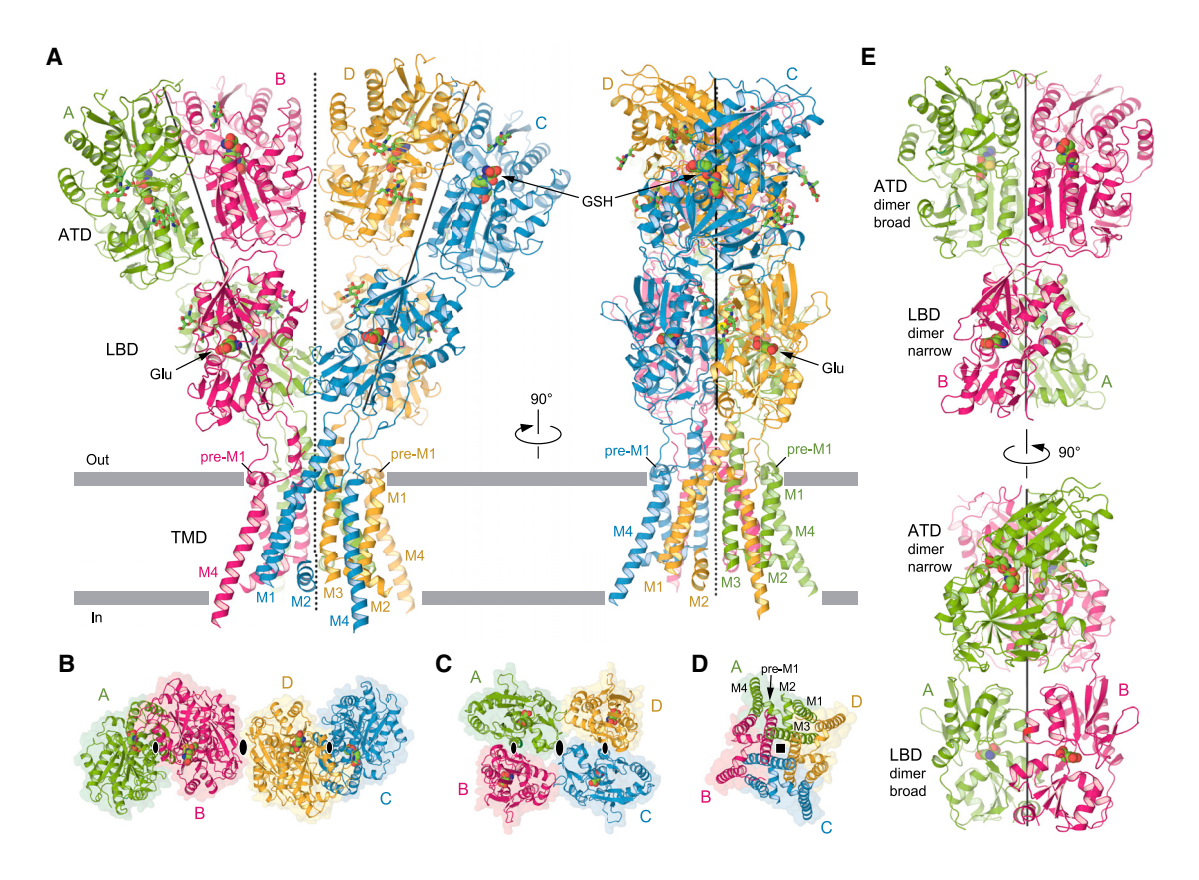


Figure 2. Overall architecture and symmetry

(A) GLR3.4 structure viewed parallel to the membrane (gray bars), with four subunits colored differently, molecules of GSH and Glu shown as space-filling models and carbohydrates as sticks. The axes of the overall and local two-fold symmetries are shown as dotted and solid lines, respectively. (B-D) ATD (B), LBD (C) and TMD (D) layers viewed extracellularly, with the overall (large ovals) and local (small ovals) two-fold and four-fold (square) symmetries indicated.

(E) ATD and LBD dimers formed by subunits A and B, viewed perpendicular to the axis of the local two-fold symmetry and showing their broad and narrow faces. See also Figures S4 and S5.

The map quality was adequate for building each subunit of the GLR3.4 tetramer, excluding the S2-M4 linkers and loops connecting M1 to M2 and M2 to M3, which were not represented clearly by resolved density.

#### **Architecture and symmetry**

The Y shape of the 175-Å-tall GLR3.4 structure resembles the shape of non-NMDA subtype iGluR structures (Burada et al., 2020b; Meyerson et al., 2016; Sobolevsky et al., 2009; Figure 2A). Similar to all iGluRs, the structure of GLR3.4 has a three-layer architecture, which includes the amino-terminal domain (ATD) layer at the top, the LBD layer in the middle, and the transmembrane domain (TMD) layer at the base of the "Y." The ATDs and LBDs of subunits A/B and C/D form dimers with monomers related by two-fold rotational symmetry. The GLR3.4 tetramer has an overall two-fold rotational symmetry that relates one ATD dimer to another, one LBD dimer to the second, and half of the TMD to another half. The axes of local two-fold rotational symmetry for the LBD and ATD dimers coincide and make a 20° angle with the axis of the overall two-fold rotational symmetry of the tetramer. This is very different from the domain organization of AMPA, kainate, and NMDA subtypes of iGluRs, where the ATD and LBD dimers have distinct axes of local two-fold rotational symmetry. An even more striking feature of GLR3.4 architecture is the lack of domain swapping between the ATD and LBD dimers, which is an inherent property of all major iGluR subtypes. The only exception among iGluRs are orphan delta receptors, which have been recently proposed to follow non-swapped domain architecture similar to GLR3.4 on the basis of low-resolution cryo-EM reconstructions (Burada et al., 2020a, 2020b).

We confirmed the unorthodox subunit and domain arrangement of GLR3.4 by introducing cysteine substitutions at intersubunit interfaces and observing redox-dependent dimer formation as a result of spontaneous subunit crosslinking (Figure S4). There are five intersubunit interfaces that keep the four GLR3.4 subunits together by means of hydrogen bonds and hydrophobic and ionic interactions (Figure S4). In the ATD layer, the intradimer interfaces between subunits A and B as well as C and D are large (3,180 Å<sup>2</sup>) and involve both the upper (L1) and lower (L2) lobes. In contrast, the interdimer interface between subunits B and D, which is mediated primarily by ionic interactions between R436 and E431, is small (209 Å<sup>2</sup>) but keeps the A/B and C/D dimers from falling apart. Similarly, in the LBD layer, the intradimer interfaces between subunits A and B as well as C and D are large (800 Å<sup>2</sup>), while



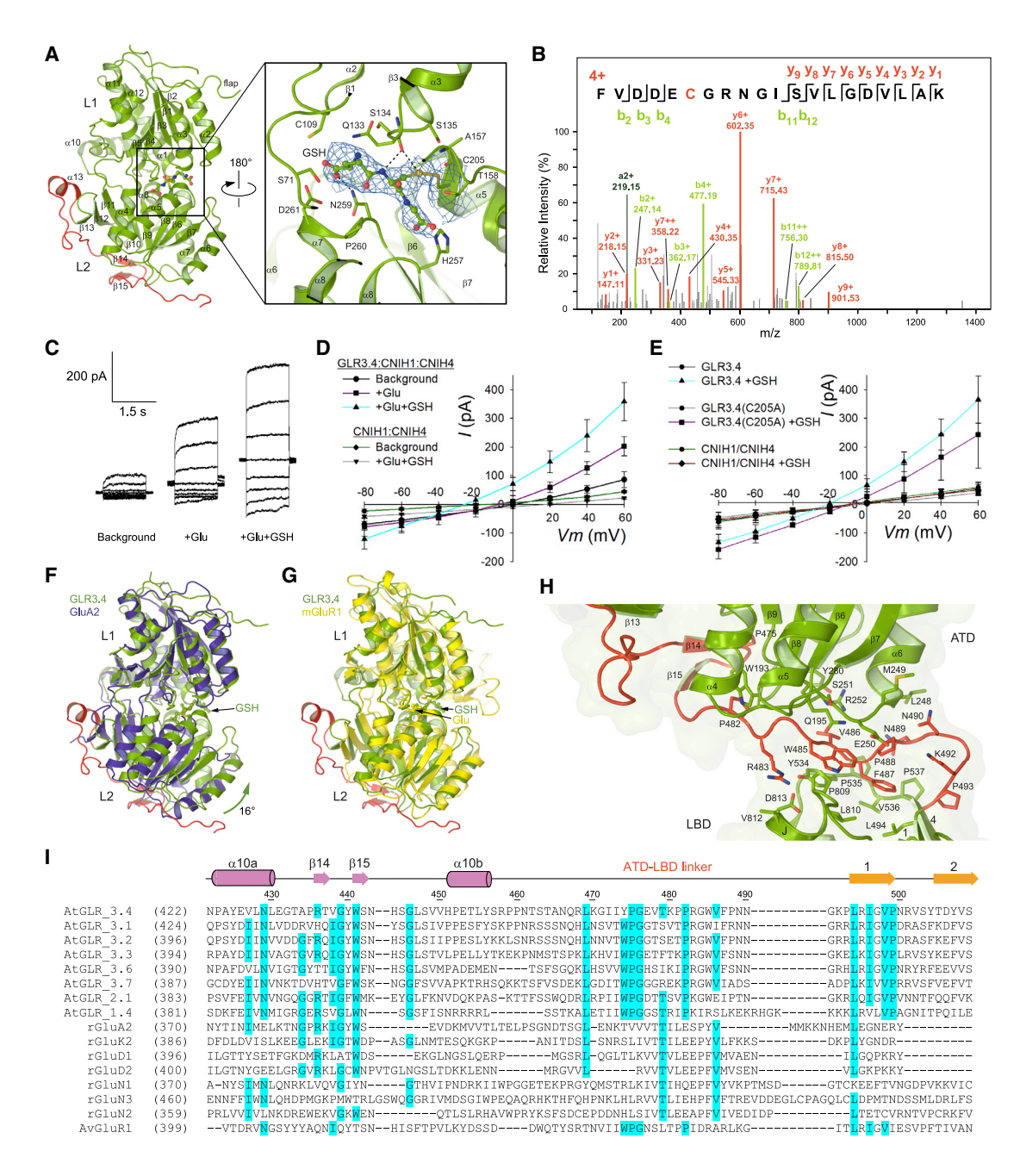


Figure 3. Amino-terminal domain

(A) Structure of the GLR3.4 ATD with secondary structure elements labeled. The ATD-LBD linker domain is colored red. The inset shows a close-up view of the GSH binding pocket. GSH is covalently bound to C205 and shown in ball-and-stick representation. Binding pocket residues are shown as sticks, and their interactions with GSH are indicated by dashed lines. Density for GSH is shown as a blue mesh.

(B) Spectrum annotation of the peptide containing C205 modified by GSH.

(C) Representative whole-cell patch-clamp recordings from COS-7 cells expressing GLR3.4:CNIH1:CNIH4 prior to treatment (background; without exogenous GSH or Glu), after application of 1 mM Glu (+Glu) or after application of 1 mM Glu and 1 mM GSH together (+Glu+GSH).

(D) Voltage dependencies of currents recorded from COS-7 cells expressing GLR3.4:CNIH1:CNIH4 (like those shown in C) in comparison with the ones recorded from COS-7 cells expressing CNIH1 and CNIH4 only, before and after application of 1 mM Glu and 1 mM GSH (n = 8 for GLR3.4 background condition, n = 5 for GLR3.4 +Glu, n = 5 for GLR3.4+Glu+GSH, n = 5 for CNIH1:CNIH4 background, and n = 5 for CNIH1:CNIH4+Glu+GSH).

(E) Voltage dependencies of currents recorded from COS-7 cells expressing wild-type GLR3.4 (n = 6), GLR3.4(C205A) (n = 4), and CNIH1: CNIH4 (n = 5) before and after application of 1 mM GSH. Both wild-type and mutant GLR constructs were co-transfected with CNIH1 and CNIH4. All data shown in (D) and (E) are mean ± SEM.

(legend continued on next page)

### **Molecular Cell**

### Article



the interdimer interface between subunits A and C is small (218 Å<sup>2</sup>) and mediated by hydrogen bonds between T717 and N719. The four GLR3.4 subunits interact most extensively at the TMD, where each of the four pairs of the neighboring subunits (A/B, B/C, C/D, and D/A) contribute a large  $(1,547 \text{ Å}^2)$  intersubunit interface. Apart from numerous hydrophobic interactions, which are typical for transmembrane regions, these interfaces are also stabilized by hydrogen bonds between residues T613, E615, L686, N689, S690, T693, T697, S698, L700, K856, and S857 that belong to the adjacent subunits.

The symmetrical dimer-of-dimers organization of GLR3.4 is maintained over the ATD and LBD layers (Figures 2B and 2C) but changes to pseudo-four-fold symmetrical organization in the TMD layer (Figure 2D). Correspondingly, interfaces among four GLR3.4 subunits are equivalent at the level of TMD but distinct between the ATDs and LBDs, with only the proximal pairs contributing to the interdimer interfaces. Interestingly, the pairs of proximal and distal subunits in GLR3.4 are exactly the same as in iGluRs' swapped topology, despite the lack of domain swapping between the ATD and LBD layers. Indeed, the A/C pair is distal in the ATD layer and proximal in the LBD layer, while the B/D pair is proximal in the ATD layer and distal in the LBD layer (Figures 2B and 2C). Switching of the proximal and distal subunit pairs becomes possible because of the perpendicular orientation of the ATD and LBD dimers with respect to each other (Figure 2E).

The overall two-fold rotational symmetry of the GLR3.4 tetramer with pseudo-four-fold symmetrical TMD (Figure 2D) is a result of two diagonal pairs, A/C and B/D, of chemically identical subunits adapting two different conformations (Figure S5A). Although their extracellular domains related by the local two-fold rotational symmetry have the same conformations, their TMDs are displaced in a 93° rotation (Figure S5B). As a result of such dramatic conformational changes, the A/C and B/D subunit pairs play different structural roles in the extracellular portion of GLR3.4, while contributing equally to the ion channel. As a reflection of the different structural roles of the A/C and B/D subunit pairs, the subunits B and D ATDs are in direct contact, while the subunits A and C ATDs are separated by more than 70 Å (Figures S5C and S5D).

#### **ATDs**

The ATDs of GLR3.4 adapt a clamshell architecture that was previously observed in the ATDs of iGluRs (Hansen et al., 2010), bacterial periplasmic amino acid binding proteins (Trakhanov et al., 2005), the extracellular domain of the natriuretic peptide receptor (He et al., 2001), and the LBDs of family C G proteincoupled receptors, including metabotropic glutamate (Koehl et al., 2019) and GABAB receptors (Papasergi-Scott et al., 2020; Park et al., 2020; Shaye et al., 2020). The dimer-of-dimers assembly of ATDs in iGluRs is important for their tetrameric stability, but functionally these domains are orphan in AMPA and kainate subtypes because of their open clamshells that have not been reported to bind to any ligand and pronounced interfaces between the upper L1 and lower L2 lobes that restrain clamshell opening/closing transformations (Jin et al., 2009). NMDA receptors, which bind the inhibitor zinc ion inside the GluN2B subunit ATD clamshell and conduct the conformational changes in the ATDs to the LBDs and the ion channel (Jalali-Yazdi et al., 2018; Karakas et al., 2009), are an exception. As the overall domain organization and shape of GLR3.4 resembles more AMPA and kainate than NMDA receptors, we expected the ATD clamshells to be similar to non-NMDA receptors. Against these expectations, we found that the GLR3.4 ATDs are all bound to glutathione (GSH) through S-glutathionylation of cysteine C205 (Figure 3A).

The binding of GSH in the middle of the ATD clamshell explains why GSH has been previously described as an activator of GLRs (Qi et al., 2006). The reversible covalent linking to cysteine C205 endows GSH with the potential to act as a biological switch and be integral in several critical oxidative signaling events (Xiong et al., 2011), including stress response in plants (Dixon et al., 2005). Apart from its disulfide bond to C205, GSH is held in its binding pocket by hydrogen bonds to the backbone carbonyl of Q133 and the amide nitrogen of N259 as well as several non-bonded contacts. As a result of all these interactions, GSH binding is strong, signified by the clearly resolved density that unambiguously identifies the position and pose of this molecule in its binding pocket (Figure 3A, inset). Covalent modification of C205 by GSH was also confirmed by the standard bottom-up proteomics approach (Figure 3B). Wild-type GLR3.4 and C205A mutant protein samples digested in reducing and nonreducing conditions were subjected to mass spectrometry analysis. Samples digested in reducing conditions showed no GSH modification. However, when the digest was carried out in non-reducing conditions, GSH was detected at the residue 205 in the wild-type protein but not in the C205A mutant.

We tested a potential role of GSH in GLR3.4 function by heterologously expressing the channel in COS-7 cells. When GLR3.4 was co-expressed with CNIH1 and CNIH4, Glu with GSH elicited larger currents than Glu alone (Figures 3C and 3D). This activating effect of GSH was impaired by C205A mutation (Figure 3E), suggesting that cysteine C205 and the GSH binding pocket identified in the ATD play an important role in GLR3.4 function. On the other hand, significant GSH-induced potentiation of GLR3.4(C205A) currents indicates that there is a

(F and G) Superposition of the GLR3.4 ATD with GluA2 ATD (blue; PDB: 3H5V) (F) and mGluR1 ligand-binding domain (yellow; PDB: 1EWK) (G). Closure by 16° of the GLR3.4 ATD clamshell compared with the GluA2 ATD clamshell is indicated by the green arrow.

<sup>(</sup>H) Close-up view of the GLR3.4 interface between ATD and LBD, with the contributing residues shown as sticks.

<sup>(</sup>I) Amino acid sequence alignment for the ATD-LBD linker region of AtGLR3.4 (NP\_001030971.1), AtGLR3.1 (NP\_028351.2), AtGLR3.2 (NP\_567981.1), AtGLR3.3 (NP\_174978.1), AtGLR3.6 (NP\_190716.3), AtGLR3.7 (NP\_565744.1), AtGLR2.1 (NP\_198062.2), AtGLR1.4 (NP\_187408.2), AMPA subtype rat GluA2 (NP\_058957), kainate subtype rat GluK2 (P42260.2), delta subtype rat GluD1 (NP\_077354.1) and GluD2 (NP\_077355.1), NMDA subtype rat GluN1 (EDL93606.1), GluN3A (NP\_612555.1), and GluN2A (NP\_036705.3), and AvGluR1 (ADW94593.1). Numbering is for the mature protein. Secondary structure elements are shown as cylinders (α helices), arrows (β strands), and lines (loops) and colored according to domains, ATD (purple) and LBD (orange). Conserved residues are highlighted in blue.

### CellPress

### **Molecular Cell** Article

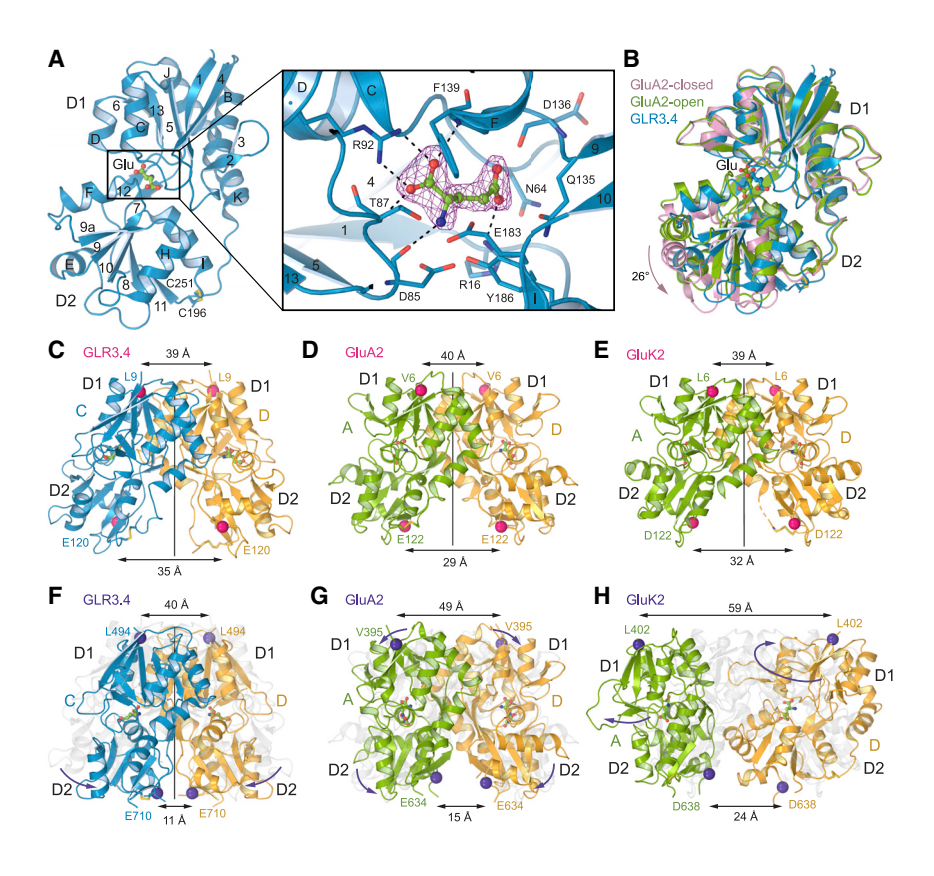


### Figure 4. Ligand-binding domain

(A) Structure of the Glu-bound isolated GLR3.4 LBD with secondary structure elements labeled. The inset shows a close-up view of the Glu binding pocket, with Glu shown in ball-and-stick representation and the omit map density for Glu at 50 shown as purple mesh. Binding pocket residues are shown as sticks, and their interactions with Glu are indicated by dashed lines.

(B) Superposition of the Glu-bound isolated GLR3.4 LBD (blue) with Glu-bound isolated GluA2 LBD (green; PDB: 1FTJ) and isolated apo-state GluA2 LBD (pink; PDB: 1FTO). Opening of the apostate GluA2 LBD clamshell by 26° compared with the Glu-bound LBD clamshells is indicated by the pink arrow.

(C-E) Glu-bound dimers of isolated GLR3.4 LBD (C), GluA2 LBD (PDB: 1FTJ) (D), and GluK2 LBD (PDB: 3G3F) (E), with the distances between upper and lower lobes indicated. The two-fold symmetry axes are shown as vertical black lines.

(F-H) LBD dimers from the full-length structures of GLR3.4 (F), GluA2 in complex with GSG1L (PDB: 5VHZ) (G), and GluK2 (PDB: 5KUF) (H), in complex with Glu, L-quisqualate, and 2S,4R-4-methylglutamate, respectively, and superposed with the corresponding isolated LBD dimers (C-E) shown in gray. Rearrangements of LBDs in the full-length structures compared with isolated LBDs are indicated by purple arrows.

See also Figure S6 and Table S2.

C205A-independent component of activation by GSH. For example, this component can be mediated by GSH binding to the same site in the ATD but without covalent attachment to C205.

To infer whether GSH binding has the potential to produce conformational changes in the GLR3.4 protein, we compared its ATD to the ATD of the AMPA subtype iGluR GluA2, which has the same overall fold but does not bind to any ligands. Strikingly, GSH-bound clamshell of the GLR3.4 ATD is 16° more closed than the ATD clamshell of GluA2 (Figure 3F). This conformation is reminiscent of the conformation of mGluR LBD after it closes in response to the binding of agonist glutamate (Figure 3G). Thus, a comparison of the GLR3.4 ATD with the domains of a similar fold suggests that GSH binding can cause conformational changes in the GLR protein, which might contribute to gating of its ion channel.

For conformational changes in the ATD to be effectively transmitted to the LBD and TMD, the ATD must have a strong structural connection to the LBD, such as the one observed in NMDA receptors (Karakas and Furukawa, 2014; Lee et al., 2014) and which is largely missing in AMPA, kainate, or delta receptors (Burada et al., 2020b; Meyerson et al., 2016; Sobolevsky et al., 2009). In GLR3.4, a unique ATD-LBD linker plays the role of an inter-domain connector, creating a strong interface between the ATD and LBD through a network of hydrophobic (residues W485, F487, L494, Y534, P535, V536, P809, and L810) and electrostatic (residues L248, R483, N489, N490, Y534, P535, P809, and D813) interactions (Figure 3H). Such a strong connection between the ATD and LBD ensures that conformational changes in the ATD are allosterically transmitted to the LBD. This interaction appears highly specific to GLRs, as the ATD-LBD linker amino acid sequence alignment shows low similarity between GLRs and iGluRs (Figure 3I). On the other hand, the majority of residues in the ATD-LBD linker are conserved among GLRs and highly conserved among clade 3 GLRs (Figure 3I).

LBDs are typically the drivers of conformational changes in iGluRs that start with agonist binding to the LBD and end up with the opening of the ion channel for current conductance. To get a high-resolution view of GLR3.4 LBD and ligand binding, we purified this domain separately and solved crystal structures of the isolated LBD in complex with agonists glutamate, serine, and methionine (Table S2). The structure of GLR3.4 LBD has a clamshell architecture (Figure 4A; Figures S6A-S6C) that is typical for iGluRs and similar to the recently published structures of isolated GLR3.2 and GLR3.3 LBDs (Figure S6D). The agonist binds in the middle of the LBD clamshell, to the binding site between its upper D1 and lower D2 lobes, resulting in a closed clamshell conformation (Figure 4B), and agonist binding can be monitored using microscale thermophoresis (Figure S6E). The serine-bound LBD structure was solved without adding the ligand to the protein, indicating serine's endogenous origin (see STAR Methods). Accordingly, in thermophoresis experiments, serine binding was not detected, likely because it was already bound to the LBD (Figure S6E). As a consequence, the

### Article



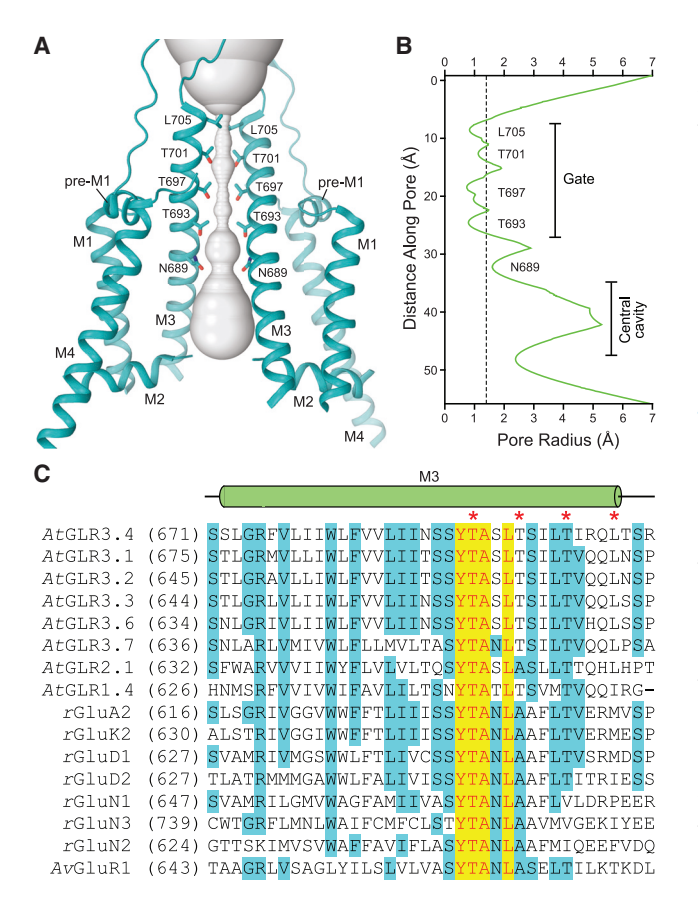


Figure 5. Ion channel

(A) Ion conduction pathway (gray) in GLR3.4, with residues lining the pore shown as sticks. Only two of four GLR3.4 subunits are shown, with the front and back subunits removed for clarity.

(B) Pore radius calculated using HOLE. The dashed line corresponds to 1.4 Å (radius of a water molecule).

(C) Amino acid sequence alignment for the M3 region of GLRs and iGluRs. The gate-forming residues are indicated by asterisks.

apparent dissociation constants for glutamate and methionine unlikely report their true affinities but rather effective concentrations to outcompete endogenous serine.

The key interactions with agonists and binding residues are conserved among iGluRs and GLRs (Alfieri et al., 2020; Gangwar et al., 2021). For all three agonists, the guanidinium group of R92 (R577 in the full-length GLR3.4) and the backbone amines of T87 and F139 are hydrogen bonded to the carboxyl group of the ligand, while the backbone carbonyl oxygen of D85, the hydroxyl groups of T87 and Y186, and the carboxyl group of E183 coordinate the amino group of the ligand. The ligand side chains are stabilized differently. The side-chain carboxyl group of glutamate and the thioether group of methionine are additionally coordinated by the guanidinium group of R16, amide groups of N64 and Q135, the phenol group of Y67, and the backbone carbonyl oxygen of D136 (Figure 4A, inset; Figure S6C). These interactions are missing in the case of serine, which lacks the bulky side chain. Instead, a water molecule occupies the void, where it is stabilized by hydrogen bonds with the hydroxymethyl side chain of serine, the guanidinium group of R16, the amide group of Q135, and the backbone carbonyl oxygen of D136 (Figure S6B). Water molecules played a similar role in the binding of glycine to the LBDs of GLR3.2 and GLR3.3 (Alfieri et al., 2020; Gangwar et al., 2021). Altogether, these data illustrate how the ligandbinding pocket of GLRs evolved to bind differently sized amino acids by exploiting the same interactions for binding the conserved amino acid core and adjusting the fit of the side chains with water. This explains the ligand-binding promiscuity of GLRs, which are activated by at least 12 of the 20 proteinogenic amino acids and the non-proteinogenic amino acid ACC (1-aminocyclopropane-1-carboxylic acid) (Forde and Roberts, 2014; Kong et al., 2016; Michard et al., 2011; Mou et al., 2020; Tapken et al., 2013; Vincill et al., 2012; Vincill et al., 2013; Wudick et al., 2018a, 2018b), in contrast to vertebrate iGluRs, which are activated only by specific amino acids (Traynelis et al., 2010). Interestingly, ACC was shown to be a partial agonist for the NMDA receptor GluN1 subunit (Inanobe et al., 2005), while invertebrate iGluRs can also be activated by different amino acids (Lomash et al., 2013).

In our crystal structures, the isolated LBDs form dimers that show back-to-back arrangement of monomers (Figure 4C), typical for the open-state LBD dimers in iGluRs. Indeed, the dimers are held together through D1-D1 interfaces, reminiscent of GluA2 (Figure 4D), and GluK2 (Figure 4E) LBD dimers. Interestingly, the LBD dimers in the context of full-length GLR3.4 show a very different assembly of monomers, with about the same distance between the upper lobes as in the isolated LBD structures but a much shorter distance between their bottom lobes (Figure 4F). The reduced separation of the D2 lobes in dimers of agonist-bound LBDs is the characteristic feature of the iGluR desensitized state (Figures 4G and 4H). In contrast to the open state, which also has LBD clamshells closed with agonists, the desensitized state is characterized by a non-conducting ion channel.

#### Ion channel

Similar to iGluRs, the ion channel of GLR3.4 is assembled of the TMDs of four subunits in a four-fold symmetrical manner, each TMD contributing the transmembrane helices M1, M3, and M4 and a re-entrant intracellular loop M2 (Figures 2D and 5A). The extracellular part of the channel's ion conduction pathway is lined by the M3 helices that form the gate. Its intracellular part, which is typically responsible for ion selectivity, is lined by the non-helical portions of M2, apparently disordered in our cryo-EM maps. M1 and M4 are on the periphery of the ion channel and contact the surrounding TMD membrane lipid. M1 helices are preceded by the short pre-M1 helices that form an extracellular collar around the ion permeation pathway, which in AMPA receptors harbors binding sites for non-competitive inhibitors, including the antiepileptic drug perampanel (Yelshanskaya et al., 2016).

Measurements of the pore radius (Figures 5A and 5B) suggest that the ion channel is in the closed non-conducting conformation. The pore's narrow constriction is formed by the extracellular portions of the M3 helices, specifically by four rings of residues, including T693, T697, T701, and L705. The homologous residues in iGluRs that also form the pore's narrow constriction are either



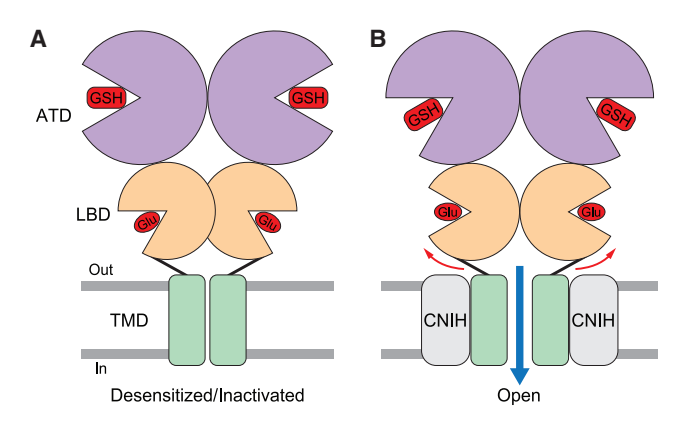


#### Figure 6. GLR3.4 gating

(A) In the absence of CNIHs (HEK and COS-7 cells), GLR3.4 adapts desensitized or inactivated conformation, where GSH is bound to ATD (purple), Glu is bound to LBD (orange), and the channel (green) is in closed, non-conducting conformation.

(B) In the presence of CNIHs (gray, COS-7 cells), ligand-induced conformational changes in the extracellular domain (red arrows) can lead to opening of the ion channel and ion conductance (blue arrow).

part of the highly conserved SYTANLAAF motif or just C-terminal to it (Figure 5C). The distinct character of gate-forming residues in GLR3.4 compared with iGluRs suggest that gating and permeation properties of GLRs might differ from iGluRs.

### **DISCUSSION**

In the GLR3.4 structure, the ATDs (Figure 3) and LBDs (Figure 4) are bound to agonist molecules. The ATDs are bound to GSH and adapt closed clamshell conformations. The LBDs also adapt closed clamshell conformations and are modeled bound to Glu, which we added to the protein before subjecting it to cryo-EM. There is a possibility, however, that the LBDs in the full-length GLR3.4 structure are bound to Ser, similar to the isolated LBD, which was found bound to Ser of endogenous origin (Figure S6; STAR Methods). In fact, it is practically impossible to distinguish Glu from Ser in cryo-EM maps at 3.57 Å resolution (Figures 1 and S3; Video S1). Independent of whether the LBDs are bound to Glu or Ser, their closed clamshell conformations are identical (Figure S6A).

Closed clamshell conformations observed for the ATDs and LBDs are active conformations of the clamshell domains, which can drive the opening of the GLR3.4 ion channel. However, the ion channel in the GLR3.4 structure is in a closed non-conducting state (Figure 5), suggesting that the structure represents a desensitized or inactivated state. This conclusion is supported by the arrangement of monomers in the GLR3.4 LBD dimers, where the lower lobes D2 are separated by a much smaller distance (Figure 4F) than expected from dimers representing the active state (Figures 4C-4E), recently confirmed by the openstate structures of the intact AMPA receptor (Chen et al., 2017; Twomey et al., 2017). Consistently, the smaller separation of the D2 lobes was also observed in the desensitized states of AMPA (Figure 4G) and kainate (Figure 4H) receptors. The conformational state of the GLR3.4 structure, therefore, suggests common features of the gating mechanisms of GLRs and iGluRs. At the level of LBD, gating is triggered by the binding of agonist that presumably leads to individual clamshell closures and separation of the D2 lobes (Figure 6). Applied to the LBD-TMD linkers, the separation of the D2 lobes would cause ion channel opening. During desensitization, the monomers of the LBD dimers could rearrange to decrease the distance between the D2 lobes, relieve the strain on the LBD-TMD linkers and convert the channel to the closed non-conducting state.

Despite the apparent similarities in the general principles of gating between GLRs and iGluRs, there are substantial differences. First, in COS-7 cells, GLR3.4 requires CNIHs to conduct currents (Figure 1; Figure S2). The majority of iGluRs conduct currents in the absence of CNIHs, although surface expression and gating of AMPA-subtype iGluRs are strongly regulated by CNIHs (Nakagawa, 2019; Schwenk et al., 2009). The only iGluR exception is GluD-subtype channels, which alone conduct currents only if they acquire mutations in the pore region (Kohda et al., 2000; Yadav et al., 2011). Interestingly, these silent iGluRs are the only iGluRs that share GLR3.4's non-swapped arrangement of ATD and LBD domains (Burada et al., 2020a, 2020b). Whether GluDs can mediate currents by binding to CNIHs or other auxiliary subunits remains undiscovered. Similarly, the possible roles of CNIHs in GLR trafficking to the cell surface and acting as chaperones to alter subunit conformations and assembly will require further investigation.

Second, agonist molecules can bind not only to the LBD but also to the ATD (Figure 3), suggesting that GLR3.4's channel opening can be triggered from both extracellular domain layers (Figure 6). The unique architecture of GLR3.4 with non-swapped pairs of the ATD and LBD dimers and tight ATD-LBD linkage through the connecting domain is likely important for transmitting conformational changes in the ATD and LBD layers to the ion channel. Similarly, the unique GLR3.4 architecture allows the arrangement of monomers within the LBD dimers, which is clearly different from AMPA and kainate receptors (Figures 4F-4H). Accordingly, the distinct conformational ensemble may be an indication that GLRs and iGluRs have principally different desensitization mechanisms. Additional structural and functional studies are necessary to decipher the GLR gating mechanisms, its regulation by CNIHs, and the way it shapes GLRs' functions in plants.

### Limitations of the study

According to our experiments, function of GLR3.4 requires CNIH auxiliary subunits. In contrast, our full-length structure of GLR3.4 is determined in the absence of CNIH subunits. Solving structures of GLR3.4-CNIH complexes will be necessary to confirm the physiological relevance of the GLR3.4 structure and to better understand the molecular bases of GLR3.4 function. Our fulllength structure of GLR3.4 reports only a single conformation, which we interpret as a desensitized state. We propose that GLR3.4 can undergo conformational changes and open its ion channel to carry out GLR3.4 physiological functions. To verify this hypothesis and to characterize gating and conformational ensemble of GLR3.4 more completely, it will be necessary to solve structures of GLR3.4 and GLR3.4-CNIH complexes in the closed and open states. The unique modulation of GLR3.4

### **Molecular Cell**

### **Article**



function by GSH binding to the ATD is particularly interesting, as it has not been observed in iGluRs. To understand the molecular mechanism of this modulation, it will be necessary to solve structures of GLR3.4 and GLR3.4-CNIH complexes in the absence of bound GSH.

#### **STAR**\*METHODS

Detailed methods are provided in the online version of this paper and include the following:

- KEY RESOURCES TABLE
- RESOURCE AVAILABILITY
  - Lead contact
  - Materials availability
  - Data and code availability
- EXPERIMENTAL MODEL AND SUBJECT DETAILS
- METHOD DETAILS
  - Constructs
  - Plant transformation
  - GLR3.4-S1S2 expression and purification
  - GLR3.4-S1S2 crystallization and structure determi-
  - O Measurements of ligand binding to GLR3.4-S1S2 using microscale thermophoresis
  - Full-length GLR3.4 expression and purification
  - Cryo-EM sample preparation and data collection
  - Image processing
  - Model building
  - Cysteine crosslinking
  - COS-7 cells transfection and Ca<sup>2+</sup> imaging
  - Patch-clamp recordings
  - O Extracellular calcium influx measurements
  - Confocal microscopy of Arabidopsis pollen
  - Liquid chromatography and mass spectrometry
- QUANTIFICATION AND STATISTICAL ANALYSIS

### SUPPLEMENTAL INFORMATION

Supplemental information can be found online at https://doi.org/10.1016/j. molcel.2021.05.025.

### **ACKNOWLEDGMENTS**

We thank R. Grassucci, Z. Zhang, Y.-C. Chi, and L. Zheng (Columbia University Cryo-Electron Microscopy Center) for help with microscope operation and cryo-EM data collection; Surajit Banerjee (beamline 24-ID-C of the Advanced Photon Source) for assistance with crystallographic data collection; Rajesh Kumar Soni (Proteomics and Macromolecular Crystallography Shared Resource, Herbert Irving Comprehensive Cancer Center, Columbia University) for mass spectrometry data acquisition; and Renato Bruni (New York Structural Biology Center) for help with microscale thermophoresis (MST). The crystallographic data were collected at beamline 24-ID-C of the Advanced Photon Source, one of the Northeastern Collaborative Access Team beamlines, which are funded by the National Institute of General Medical Sciences of the National Institutes of Health (P30 GM124165). The Pilatus 6M detector on the 24-ID-C beamline is funded by an NIH Office of Research Infrastructure Programs (ORIP) High-End Instrumentation (HEI) grant (S10 RR029205). A.I.S. was supported by the NIH (R01 CA206573, R01 NS083660, and R01 NS107253) and the National Science Foundation (NSF) (1818086). J.A.F. was supported by the NIH (R01 GM131043) and the NSF (MCB1714993 and

MCB1930165). M.M.W. was supported by Deutsche Forschungsgemeinschaft (DFG; 267205415- SFB 1208). The graphical abstract was made with the Arabidopsis thaliana image adapted from BioRender.com.

#### **AUTHOR CONTRIBUTIONS**

M.N.G. and S.P.G. made constructs and prepared protein samples for crystallography and cryo-EM and carried out cryo-EM data collection and processing. S.P.G. carried out crystallographic data collection and processing. S.P.G. and A.I.S. built molecular models. M.N.G. made constructs for crosslinking experiments. M.N.G., O.K., and M.V.Y. prepared protein samples. M.N.G. carried out the crosslinking experiments. O.K. performed mass spectrometry experiments and data analysis. J.A.F., A.A.S., and E.M. conceived physiological experiments, E.M., J.B.-C., M.A.L., and A.A.S. carried out patch-clamp recordings and calcium imaging, M.M.W. and M.A.L. performed GFP imaging, genotyping, and phenotyping characterization of wild-type and mutant Atlgr3.4 in plants and pollen. M.T.P. carried out vibrating-probe calcium flux measurements in pollen tubes. M.N.G., S.P.G., E.M., A.A.S., O.K., M.V.Y., J.A.F., and A.I.S. wrote the manuscript.

#### **DECLARATION OF INTERESTS**

The authors declare no competing interests.

Received: April 2, 2021 Revised: April 23, 2021 Accepted: May 19, 2021 Published: June 22, 2021

#### **REFERENCES**

Adams, P.D., Afonine, P.V., Bunkóczi, G., Chen, V.B., Davis, I.W., Echols, N., Headd, J.J., Hung, L.W., Kapral, G.J., Grosse-Kunstleve, R.W., et al. (2010). PHENIX: a comprehensive Python-based system for macromolecular structure solution. Acta Crystallogr. D Biol. Crystallogr. 66, 213-221.

Afonine, P.V., Grosse-Kunstleve, R.W., Echols, N., Headd, J.J., Moriarty, N.W., Mustyakimov, M., Terwilliger, T.C., Urzhumtsev, A., Zwart, P.H., and Adams, P.D. (2012). Towards automated crystallographic structure refinement with phenix.refine. Acta Crystallogr. D Biol. Crystallogr. 68, 352-367.

Alfieri, A., Doccula, F.G., Pederzoli, R., Grenzi, M., Bonza, M.C., Luoni, L., Candeo, A., Romano Armada, N., Barbiroli, A., Valentini, G., et al. (2020). The structural bases for agonist diversity in an Arabidopsis thaliana glutamate receptor-like channel. Proc. Natl. Acad. Sci. U S A 117, 752-760.

Armstrong, N., and Gouaux, E. (2000). Mechanisms for activation and antagonism of an AMPA-sensitive glutamate receptor: crystal structures of the GluR2 ligand binding core. Neuron 28, 165-181.

Armstrong, N., Sun, Y., Chen, G.Q., and Gouaux, E. (1998). Structure of a glutamate-receptor ligand-binding core in complex with kainate. Nature 395,

Burada, A.P., Vinnakota, R., and Kumar, J. (2020a). The architecture of GluD2 ionotropic delta glutamate receptor elucidated by cryo-EM. J. Struct. Biol. 211, 107546.

Burada, A.P., Vinnakota, R., and Kumar, J. (2020b). Cryo-EM structures of the ionotropic glutamate receptor GluD1 reveal a non-swapped architecture. Nat. Struct. Mol. Biol. 27, 84-91.

Chen, S., McMullan, G., Faruqi, A.R., Murshudov, G.N., Short, J.M., Scheres, S.H., and Henderson, R. (2013). High-resolution noise substitution to measure overfitting and validate resolution in 3D structure determination by single particle electron cryomicroscopy. Ultramicroscopy 135, 24-35.

Chen, S., Zhao, Y., Wang, Y., Shekhar, M., Tajkhorshid, E., and Gouaux, E. (2017). Activation and desensitization mechanism of AMPA receptor-TARP complex by cryo-EM. Cell 170, 1234-1246.e14.

Chi, H., Liu, C., Yang, H., Zeng, W.F., Wu, L., Zhou, W.J., Wang, R.M., Niu, X.N., Ding, Y.H., Zhang, Y., et al. (2018). Comprehensive identification of



### **Molecular Cell**

peptides in tandem mass spectra using an efficient open search engine. Nat. Biotechnol. 36, 1059-1061.

De Bortoli, S., Teardo, E., Szabò, I., Morosinotto, T., and Alboresi, A. (2016). Evolutionary insight into the ionotropic glutamate receptor superfamily of photosynthetic organisms. Biophys. Chem. 218, 14-26.

DeLano, W.L. (2002). The PyMOL Molecular Graphics System (San Carlos, CA: DeLano Scientific).

Dixon, D.P., Skipsey, M., Grundy, N.M., and Edwards, R. (2005). Stressinduced protein S-glutathionylation in Arabidopsis. Plant Physiol. 138,

Emsley, P., and Cowtan, K. (2004). Coot: model-building tools for molecular graphics. Acta Crystallogr. D Biol. Crystallogr. 60, 2126-2132.

Forde, B.G., and Roberts, M.R. (2014). Glutamate receptor-like channels in plants: a role as amino acid sensors in plant defence? F1000Prime Rep. 6, 37.

Gangwar, S.P., Green, M.N., Michard, E., Simon, A.A., Feijó, J.A., and Sobolevsky, A.I. (2021). Structure of the Arabidopsis glutamate receptor-like channel GLR3.2 ligand-binding domain. Structure 29, 161-169.e4.

Goehring, A., Lee, C.H., Wang, K.H., Michel, J.C., Claxton, D.P., Baconguis, I., Althoff, T., Fischer, S., Garcia, K.C., and Gouaux, E. (2014). Screening and large-scale expression of membrane proteins in mammalian cells for structural studies. Nat. Protoc. 9, 2574-2585.

Hansen, K.B., Furukawa, H., and Traynelis, S.F. (2010). Control of assembly and function of glutamate receptors by the amino-terminal domain. Mol. Pharmacol. 78, 535-549.

He, X., Chow, D., Martick, M.M., and Garcia, K.C. (2001). Allosteric activation of a spring-loaded natriuretic peptide receptor dimer by hormone. Science

Inanobe, A., Furukawa, H., and Gouaux, E. (2005). Mechanism of partial agonist action at the NR1 subunit of NMDA receptors. Neuron 47, 71-84.

Jalali-Yazdi, F., Chowdhury, S., Yoshioka, C., and Gouaux, E. (2018). Mechanisms for zinc and proton inhibition of the GluN1/GluN2A NMDA receptor. Cell 175, 1520-1532.e15.

Jin, R., Singh, S.K., Gu, S., Furukawa, H., Sobolevsky, A.I., Zhou, J., Jin, Y., and Gouaux, E. (2009). Crystal structure and association behaviour of the GluR2 amino-terminal domain. EMBO J. 28, 1812-1823.

Jones, A.M., Chory, J., Dangl, J.L., Estelle, M., Jacobsen, S.E., Meyerowitz, E.M., Nordborg, M., and Weigel, D. (2008). The impact of Arabidopsis on human health: diversifying our portfolio. Cell 133, 939-943.

Kabsch, W. (2010). XDS. Acta Crystallogr. D Biol. Crystallogr. 66, 125-132.

Karakas, E., and Furukawa, H. (2014). Crystal structure of a heterotetrameric NMDA receptor ion channel. Science 344, 992-997.

Karakas, E., Simorowski, N., and Furukawa, H. (2009). Structure of the zincbound amino-terminal domain of the NMDA receptor NR2B subunit. EMBO J 28 3910-3920

Kawate, T., and Gouaux, E. (2006). Fluorescence-detection size-exclusion chromatography for precrystallization screening of integral membrane proteins. Structure 14, 673-681.

Kimanius, D., Forsberg, B.O., Scheres, S.H., and Lindahl, E. (2016). Accelerated cryo-EM structure determination with parallelisation using GPUs in RELION-2. eLife 5, e18722.

Koehl, A., Hu, H., Feng, D., Sun, B., Zhang, Y., Robertson, M.J., Chu, M., Kobilka, T.S., Laeremans, T., Steyaert, J., et al. (2019). Structural insights into the activation of metabotropic glutamate receptors. Nature 566, 79-84.

Kohda, K., Wang, Y., and Yuzaki, M. (2000). Mutation of a glutamate receptor motif reveals its role in gating and delta2 receptor channel properties. Nat. Neurosci. 3. 315-322.

Kong, D., Hu, H.C., Okuma, E., Lee, Y., Lee, H.S., Munemasa, S., Cho, D., Ju, C., Pedoeim, L., Rodriguez, B., et al. (2016). L-Met activates arabidopsis GLR Ca<sup>2+</sup> channels upstream of ROS production and regulates stomatal movement. Cell Rep. 17, 2553-2561.

Krissinel, E., and Henrick, K. (2007). Inference of macromolecular assemblies from crystalline state. J. Mol. Biol. 372, 774-797.

Kucukelbir, A., Sigworth, F.J., and Tagare, H.D. (2014). Quantifying the local resolution of cryo-EM density maps. Nat. Methods 11, 63-65.

Lam, H.M., Chiu, J., Hsieh, M.H., Meisel, L., Oliveira, I.C., Shin, M., and Coruzzi, G. (1998). Glutamate-receptor genes in plants. Nature 396, 125-126.

Laskowski, R.A., Jabłońska, J., Pravda, L., Vařeková, R.S., and Thornton, J.M. (2018). PDBsum: Structural summaries of PDB entries. Protein Sci. 27,

Lee, C.H., Lü, W., Michel, J.C., Goehring, A., Du, J., Song, X., and Gouaux, E. (2014). NMDA receptor structures reveal subunit arrangement and pore architecture. Nature 511, 191-197.

Lomash, S., Chittori, S., Brown, P., and Mayer, M.L. (2013). Anions mediate ligand binding in Adineta vaga glutamate receptor ion channels. Structure

McCoy, A.J. (2007). Solving structures of protein complexes by molecular replacement with Phaser. Acta Crystallogr. D Biol. Crystallogr. 63, 32-41.

Meyerhoff, O., Müller, K., Roelfsema, M.R., Latz, A., Lacombe, B., Hedrich, R., Dietrich, P., and Becker, D. (2005). AtGLR3.4, a glutamate receptor channellike gene is sensitive to touch and cold. Planta 222, 418-427.

Meyerson, J.R., Chittori, S., Merk, A., Rao, P., Han, T.H., Serpe, M., Mayer, M.L., and Subramaniam, S. (2016). Structural basis of kainate subtype glutamate receptor desensitization. Nature 537, 567-571.

Michard, E., Lima, P.T., Borges, F., Silva, A.C., Portes, M.T., Carvalho, J.E., Gilliham, M., Liu, L.H., Obermeyer, G., and Feijó, J.A. (2011). Glutamate receptor-like genes form Ca2+ channels in pollen tubes and are regulated by pistil Dserine. Science 332, 434-437.

Michard, E., Simon, A.A., Tavares, B., Wudick, M.M., and Feijó, J.A. (2017). Signaling with ions: the keystone for apical cell growth and morphogenesis in pollen tubes. Plant Physiol. 173, 91-111.

Mou, W., Kao, Y.T., Michard, E., Simon, A.A., Li, D., Wudick, M.M., Lizzio, M.A., Feijó, J.A., and Chang, C. (2020). Ethylene-independent signaling by the ethylene precursor ACC in Arabidopsis ovular pollen tube attraction. Nat. Commun. 11, 4082.

Mousavi, S.A., Chauvin, A., Pascaud, F., Kellenberger, S., and Farmer, E.E. (2013). Glutamate receptor-like genes mediate leaf-to-leaf wound signalling. Nature 500, 422-426.

Nakagawa, T. (2019). Structures of the AMPA receptor in complex with its auxiliary subunit cornichon. Science 366, 1259-1263.

Ortiz-Ramírez, C., Michard, E., Simon, A.A., Damineli, D.S.C., Hernández-Coronado, M., Becker, J.D., and Feijó, J.A. (2017). Glutamate receptor-like channels are essential for chemotaxis and reproduction in mosses. Nature 549, 91-95,

Papasergi-Scott, M.M., Robertson, M.J., Seven, A.B., Panova, O., Mathiesen, J.M., and Skiniotis, G. (2020). Structures of metabotropic GABA<sub>B</sub> receptor. Nature 584, 310-314.

Park, J., Fu, Z., Frangaj, A., Liu, J., Mosyak, L., Shen, T., Slavkovich, V.N., Ray, K.M., Taura, J., Cao, B., et al. (2020). Structure of human GABA<sub>B</sub> receptor in an inactive state. Nature 584, 304-309.

Pettersen, E.F., Goddard, T.D., Huang, C.C., Couch, G.S., Greenblatt, D.M., Meng, E.C., and Ferrin, T.E. (2004). UCSF Chimera—a visualization system for exploratory research and analysis. J. Comput. Chem. 25, 1605–1612.

Punjani, A., Rubinstein, J.L., Fleet, D.J., and Brubaker, M.A. (2017). cryoSPARC: algorithms for rapid unsupervised cryo-EM structure determination. Nat. Methods 14, 290-296.

Qi, Z., Stephens, N.R., and Spalding, E.P. (2006). Calcium entry mediated by GLR3.3, an Arabidopsis glutamate receptor with a broad agonist profile. Plant Physiol. 142, 963-971.

Rappsilber, J., Mann, M., and Ishihama, Y. (2007). Protocol for micro-purification, enrichment, pre-fractionation and storage of peptides for proteomics using StageTips. Nat. Protoc. 2, 1896-1906.

Russo, C.J., and Passmore, L.A. (2014). Electron microscopy: ultrastable gold substrates for electron cryomicroscopy. Science 346, 1377-1380.

### **Molecular Cell**

### **Article**



Scheres, S.H. (2012). RELION: implementation of a Bayesian approach to cryo-EM structure determination. J. Struct. Biol. 180, 519-530.

Schwenk, J., Harmel, N., Zolles, G., Bildl, W., Kulik, A., Heimrich, B., Chisaka, O., Jonas, P., Schulte, U., Fakler, B., and Klöcker, N. (2009). Functional proteomics identify cornichon proteins as auxiliary subunits of AMPA receptors. Science 323, 1313-1319.

Shaye, H., Ishchenko, A., Lam, J.H., Han, G.W., Xue, L., Rondard, P., Pin, J.P., Katritch, V., Gati, C., and Cherezov, V. (2020). Structural basis of the activation of a metabotropic GABA receptor. Nature 584, 298-303.

Sobolevsky, A.I., Rosconi, M.P., and Gouaux, E. (2009). X-ray structure, symmetry and mechanism of an AMPA-subtype glutamate receptor. Nature 462, 745-756.

Stephens, N.R., Qi, Z., and Spalding, E.P. (2008). Glutamate receptor subtypes evidenced by differences in desensitization and dependence on the GLR3.3 and GLR3.4 genes. Plant Physiol. 146, 529-538.

Suloway, C., Pulokas, J., Fellmann, D., Cheng, A., Guerra, F., Quispe, J., Stagg, S., Potter, C.S., and Carragher, B. (2005). Automated molecular microscopy: the new Leginon system. J. Struct. Biol. 151, 41-60.

Tapken, D., Anschütz, U., Liu, L.H., Huelsken, T., Seebohm, G., Becker, D., and Hollmann, M. (2013). A plant homolog of animal glutamate receptors is an ion channel gated by multiple hydrophobic amino acids. Sci. Signal. 6, ra47.

Teardo, E., Carraretto, L., De Bortoli, S., Costa, A., Behera, S., Wagner, R., Lo Schiavo, F., Formentin, E., and Szabo, I. (2015). Alternative splicing-mediated targeting of the Arabidopsis glutamate receptor3.5 to mitochondria affects organelle morphology. Plant Physiol. 167, 216-227.

Trakhanov, S., Vyas, N.K., Luecke, H., Kristensen, D.M., Ma, J., and Quiocho, F.A. (2005). Ligand-free and -bound structures of the binding protein (LivJ) of the Escherichia coli ABC leucine/isoleucine/valine transport system: trajectory and dynamics of the interdomain rotation and ligand specificity. Biochemistry 44, 6597-6608.

Traynelis, S.F., Wollmuth, L.P., McBain, C.J., Menniti, F.S., Vance, K.M., Ogden, K.K., Hansen, K.B., Yuan, H., Myers, S.J., and Dingledine, R. (2010). Glutamate receptor ion channels: structure, regulation, and function. Pharmacol. Rev. 62, 405-496.

Twomey, E.C., Yelshanskaya, M.V., Grassucci, R.A., Frank, J., and Sobolevsky, A.I. (2017). Channel opening and gating mechanism in AMPAsubtype glutamate receptors. Nature 549, 60-65.

Vincill, E.D., Bieck, A.M., and Spalding, E.P. (2012). Ca(2+) conduction by an amino acid-gated ion channel related to glutamate receptors. Plant Physiol. 159, 40-46.

Vincill, E.D., Clarin, A.E., Molenda, J.N., and Spalding, E.P. (2013). Interacting glutamate receptor-like proteins in phloem regulate lateral root initiation in Arabidopsis. Plant Cell 25, 1304-1313.

Waterhouse, A., Bertoni, M., Bienert, S., Studer, G., Tauriello, G., Gumienny, R., Heer, F.T., de Beer, T.A.P., Rempfer, C., Bordoli, L., et al. (2018). SWISS-MODEL: homology modelling of protein structures and complexes. Nucleic Acids Res. 46 (W1), W296-W303.

Winn, M.D., Ballard, C.C., Cowtan, K.D., Dodson, E.J., Emsley, P., Evans, P.R., Keegan, R.M., Krissinel, E.B., Leslie, A.G., McCoy, A., et al. (2011). Overview of the CCP4 suite and current developments. Acta Crystallogr. D Biol. Crystallogr. 67, 235-242.

Wudick, M.M., Michard, E., Oliveira Nunes, C., and Feijó, J.A. (2018a). Comparing plant and animal glutamate receptors: common traits but different fates? J. Exp. Bot. 69, 4151-4163.

Wudick, M.M., Portes, M.T., Michard, E., Rosas-Santiago, P., Lizzio, M.A., Nunes, C.O., Campos, C., Santa Cruz Damineli, D., Carvalho, J.C., Lima, P.T., et al. (2018b). CORNICHON sorting and regulation of GLR channels underlie pollen tube Ca. Science 360, 533-536.

Xiong, Y., Uys, J.D., Tew, K.D., and Townsend, D.M. (2011). S-glutathionylation: from molecular mechanisms to health outcomes. Antioxid. Redox Signal. 15, 233-270.

Yadav, R., Rimerman, R., Scofield, M.A., and Dravid, S.M. (2011). Mutations in the transmembrane domain M3 generate spontaneously open orphan glutamate δ1 receptor. Brain Res. 1382, 1-8.

Yelshanskaya, M.V., Singh, A.K., Sampson, J.M., Narangoda, C., Kurnikova, M., and Sobolevsky, A.I. (2016). Structural bases of noncompetitive inhibition of AMPA subtype ionotropic glutamate receptors by antiepileptic drugs. Neuron 91, 1305-1315.

Zhang, K. (2016). Gctf: Real-time CTF determination and correction. J. Struct. Biol. 193, 1-12.

Zheng, H., Cooper, D.R., Porebski, P.J., Shabalin, I.G., Handing, K.B., and Minor, W. (2017a). CheckMyMetal: a macromolecular metal-binding validation tool. Acta Crystallogr. D Struct. Biol. 73, 223-233.

Zheng, S.Q., Palovcak, E., Armache, J.P., Verba, K.A., Cheng, Y., and Agard, D.A. (2017b). MotionCor2: anisotropic correction of beam-induced motion for improved cryo-electron microscopy. Nat. Methods 14, 331-332.

Zivanov, J., Nakane, T., Forsberg, B.O., Kimanius, D., Hagen, W.J., Lindahl, E., and Scheres, S.H. (2018). New tools for automated high-resolution cryo-EM structure determination in RELION-3. eLife 7, e42166.





### **STAR**\***METHODS**

### **KEY RESOURCES TABLE**

REAGENT or RESOURCE	SOURCE	IDENTIFIER			
Chemicals, peptides, and recombinant proteins					
Ampicillin	Sigma	Cat# A8351			
Kanamycin	Fisher scientific	Cat# BP906-5			
Tetracycline	Fisher scientific	Cat# BP912			
IPTG	Zymo Research	Cat# I1001-5			
Tris	Fisher scientific	Cat# BP152-1			
NaCl	Fisher scientific	Cat# BP358-212			
L-Glutamate	Sigma	Cat# 49621			
L-Methionine	Sigma	Cat# M9625			
MgSO4	Fluka	Cat# 13143			
DNase	Sigma	Cat# DN25-1			
PMSF	Acros Organics	Cat# 215740500			
2-Mercaptoethanol (BME)	Acros Organics	Cat# 125470100			
Ni-Affinity Resin	Takara	Cat# 635660			
Imidazole	Acros Organics	Cat# 301870025			
Thrombin	Haematologic Technologies	Cat# HCT-0020			
Glycerol	Fisher scientific	Cat# BP229-4			
MES buffer	Sigma	Cat# M2933			
PEG 2000 MME	Fluka	Cat# 81321			
Ammonium Sulfate	Fisher scientific	Cat# A702-500			
Glycine	Jena Biosciences	Cat# CS-507L			
Ammonium acetate	Fisher scientific	Cat# BP326-500			
Sodium Acetate	Fisher scientific	Cat# S209-500			
CAA	Sigma-Aldrich	Cat# C0267			
TCEP	Sigma-Aldrich	Cat# C4706			
Urea	Fischer Scientific	Cat# BP169-500			
LysC	Wako Chemicals	Cat# 129-02541			
Trypsin	Promega	Cat# V5280			
Formic Acid	Sigma-Aldrich	Cat# F0507			
CDS Empore <sup>™</sup> SDB-RPS	Fischer Scientific	Cat# 13-110-023			
Dulbecco's Modified Eagle's Medium	GIBCO	Cat# 10566024			
Fetal bovine serum	GIBCO	Cat# 16140071			
Sf-900 III SFM	GIBCO	Cat# 12658027			
Freestyle 293 expression medium	GIBCO	Cat# 12338018			
DMEM media	Corning	Cat# 10-013-CV			
Sodium butyrate	ACROS Organics	Cat# 263191000			
Lipofectamine 2000	Invitrogen	Cat#11668027			
Penicillin Streptomycin Fungizone	Cytiva HyClone	Cat# SV3007901			
FugeneHD	Promega	Cat# E2311			
EGTA	Sigma	Cat# E4378			
Bis-Tris Propane	RPI	Cat# B78000100.0			
HEPES	Sigma	Cat# H3375-250G			
D-mannitol	Fisher	Cat# M120-500			
Ca-Gluconate	Sigma	Cat# C8231-100G			
Oa-Giucoliate	Оідіпа	(Continued on next page)			

(Continued on next page)

### **Article**



Continued		
REAGENT or RESOURCE	SOURCE	IDENTIFIER
Deposited data		
Coordinates of GLR3.4-S1S2-Glu	This paper	PDB: 7LZ0
Coordinates of GLR3.4-S1S2-Ser	This paper	PDB: 7LZ1
Coordinates of GLR3.4-S1S2-Met	This paper	PDB: 7LZ2
Coordinates of full-length GLR3.4	This paper	PDB: 7LZH
Cryo-EM map of full-length GLR3.4	This paper	EMD-23606
Coordinates of ATD and micelle subtracted GLR3.4	This paper	PDB: 7LZI
Cryo-EM map of ATD and micelle subtracted GLR3.4	This paper	EMD-23607
MS raw files and output tables	This paper	PXD024563
S1S2 of <i>AtGLR</i> 3.2	Gangwar et al., 2021	PDB: 6VE8
S1S2 of <i>At</i> GLR3.3	Alfieri et al., 2020	PDB: 6R8A
Experimental models: cell lines		
HEK293S GnTI	ATCC	Cat#CRL-3022
Sf9	GIBCO	Cat#12659017
COS-7	ATTC	CRL-1651
E. coli Origami B (DE3)	Novagen	Cat# 70837
Experimental models: organisms/strains		
Agrobacterium tumefaciens strain GV3101	GoldBio	CC-207-A
Arabidopsis thaliana Col-0 ecotype	ABRC	CS70000
Arabidopsis thaliana tDNA mutant Atglr3.4-1	ABRC	Salk_201768C
Arabidopsis thaliana tDNA mutant Atglr3.4-2	ABRC	Salk_079842
Recombinant DNA		
pEF1-YC3.6	Dr. Jörg Kudla lab, Univ. Muenster, Germany	N/A
pcDNA3	Invitrogen	N/A
pcDNA3-AtGLR3.4	This paper	N/A
pcDNA3-AtGLR3.4(C205A)	This paper	N/A
pCl	Promega	N/A
pCI-AtCNIH1	Wudick et al., 2018b	N/A
pCI-AtCNIH4	Wudick et al., 2018b	N/A
pDONR201	Invitrogen	N/A
pDONR201 pDONR201-AtGLR3.4(gDNA)	Invitrogen This paper	N/A N/A
	-	
pDONR201-AtGLR3.4(gDNA)	This paper Dr. Edgar Spalding, University of	N/A
pDONR201-AtGLR3.4(gDNA) pDS_EF1-XB-glr3.4-CFP	This paper Dr. Edgar Spalding, University of Wisconsin, Madison	N/A N/A
pDONR201-AtGLR3.4(gDNA) pDS_EF1-XB-glr3.4-CFP pIRES-CD8	This paper Dr. Edgar Spalding, University of Wisconsin, Madison Clontech	N/A N/A N/A
pDONR201-AtGLR3.4(gDNA) pDS_EF1-XB-glr3.4-CFP pIRES-CD8 pK7FWG2-Lat52	This paper Dr. Edgar Spalding, University of Wisconsin, Madison Clontech Wudick et al., 2018b	N/A N/A N/A
pDONR201-AtGLR3.4(gDNA) pDS_EF1-XB-glr3.4-CFP  pIRES-CD8 pK7FWG2-Lat52 pSoup	This paper Dr. Edgar Spalding, University of Wisconsin, Madison Clontech Wudick et al., 2018b	N/A N/A N/A
pDONR201-AtGLR3.4(gDNA) pDS_EF1-XB-glr3.4-CFP  pIRES-CD8 pK7FWG2-Lat52 pSoup  Oligonucleotides  AtGLR3.4 amplification primer: 5'- gtcgact	This paper Dr. Edgar Spalding, University of Wisconsin, Madison Clontech Wudick et al., 2018b Hellens, R.P.	N/A N/A N/A N/A GenBank: EU048870.1
pDONR201-AtGLR3.4(gDNA) pDS_EF1-XB-glr3.4-CFP  pIRES-CD8 pK7FWG2-Lat52 pSoup  Oligonucleotides  AtGLR3.4 amplification primer: 5'- gtcgact ccgccaccatgggatttttggtgatgataagag -3'  AtGLR3.4 amplification primer: 5'- cggca	This paper Dr. Edgar Spalding, University of Wisconsin, Madison Clontech Wudick et al., 2018b Hellens, R.P. This paper	N/A N/A N/A N/A GenBank: EU048870.1

(Continued on next page)



Continued		
REAGENT or RESOURCE	SOURCE	IDENTIFIER
B204 5' – AGGGAACAAAAGCTGGGG AATTCAGGTCACTG GATTTTGGTTT TAGG – 3'	This paper	N/A
B278 5' – CGTAATACGACTCACTATAGGGC GAATTGGGT ACC GTCGACGAGT CAGTAATAAACG – 3'	This paper	N/A
B279 5' – TCGTTCAGCTTTTTTGT ACAAACTTGTGATATCA CTAGTCT GTTAATCAGAAAAACTCAG – 3'	This paper	N/A
B394 5' – GGGGACAAGTTTGTACAAAAAAGC AGGCTTCA TGGGATTTTTGGTGATGA TAA – 3'	This paper	N/A
B395 5' – GGGGACCACTTTGTACAAG AAAGCTGGGTCAG TAATTTCGCCATGT TGTGAT – 3'	This paper	N/A
B579 5' – TGCAGATATCCATCACACT GGCGGCCGCATGG GATTTTTGGT GATGATAAGAG – 3'	This paper	N/A
B580 5' – ATAGGGCCCTCTAGATGC ATGCTCGAGTTAAGT AATTTCGCC ATGTTGTGATTGT – 3'	This paper	N/A
C328 5' – CCCGTTCCTGCCAGCCT CATCATCAACGAATA – 3'	This paper	N/A
C329 5' – CGTTGATGATGAGGCTGGCAG GAACGGGAT ATC – 3'	This paper	N/A
Software and algorithms		
Leginon	Suloway et al., 2005	https://emg.nysbc.org/redmine/projects/ leginon/wiki/Leginon_Homepage
gCTF	Zhang, 2016	https://www.mrc-lmb.cam.ac.uk/kzhang/Gctf/
Motioncor2	Zheng et al., 2017b	https://msg.ucsf.edu/em/software/ motioncor2.html
RELION 2.0	Kimanius et al., 2016	https://www2.mrc-lmb.cam.ac.uk/relion/
UCSF Chimera	Pettersen et al., 2004	https://www.cgl.ucsf.edu/chimera/
Pymol (Schrödinger)	DeLano, 2002	https://www.pymol.org/2/
PHENIX	Adams et al., 2010	https://phenix-online.org/
CCP4	Winn et al., 2011	https://www.ccp4.ac.uk/
COOT	Emsley and Cowtan, 2004	https://www2.mrc-lmb.cam.ac.uk/ Personal/pemsley/coot
XDS	Kabsch, 2010	https://xds.mr.mpg.de/
Swiss-Model	Waterhouse et al., 2018	https://swissmodel.expasy.org/
PDBsum	Laskowski et al., 2018	https://www.ebi.ac.uk/thornton-srv/ databases/cgi-bin/pdbsum/GetPage.pl? pdbcode=index.html
SigmaPlot 11.0	Systat Software Inc.	Systatsoftware.com
Origin 2015 Sr2	OriginLab Corporation	https://www.originlab.com/doc/
pFind	Chi et al., 2018	http://pfind.ict.ac.cn/
	141 1 1 111 11 000=	https://www.ebi.ac.uk/pdbe/prot_int/
PDBePISA	Krissinel and Henrick, 2007	pistart.html

(Continued on next page)

### **Molecular Cell**

### **Article**



Continued		
REAGENT or RESOURCE	SOURCE	IDENTIFIER
Other		
DeltaVision Elite Deconvolution/TIRF microscope system	GE Healthcare	Part # 53-851206-001
CF-1.2/1.3-2Au 200 mesh holey carbon grids	Protochips	Cat#CF-1.2/1.3-2Au
Gold wire	Ted Pella, Inc.	Cat#21-10
Ion Exchange Hi-Trap Q HP column	GE Healthcare	Cat# 17-1154-01
Size Exclusion Superose 10/300 column	GE Healthcare	Cat# 17-5172-01

#### **RESOURCE AVAILABILITY**

#### Lead contact

Further information and requests for the resources and reagents should be directed to and will be fulfilled by the lead contact, Alexander Sobolevsky (as4005@cumc.columbia.edu).

#### **Materials availability**

New materials listed in key resources are available upon request.

### **Data and code availability**

Cryo-EM map for full-length GLR3.4 and after ATD and micelle subtraction have been deposited to the EMDB with the accession codes EMD-23606 and EMD-23607, respectively. Coordinates for full-length GLR3.4 and after ATD and micelle subtraction have been deposited to the PDB with the accession codes 7LZH and 7LZI, respectively. Coordinates and structure factors for GLR3.4-S1S2<sub>Glu</sub>, GLR3.4-S1S2<sub>Ser</sub> and GLR3.4-S1S2<sub>Met</sub> structures have been deposited to the PDB with the accession codes 7LZ0, 7LZ1 and 7LZ2, respectively. Raw files and full output tables for mass spectrometry results are available through PRIDE repository with identifier PXD024563 (reviewer access username: reviewer pxd024563@ebi.ac.uk, password: UDehuNMe). This study did not generate new code.

### **EXPERIMENTAL MODEL AND SUBJECT DETAILS**

Expression of the full-length GLR3.4 protein was performed in HEK293S GnTI<sup>-</sup> cells (ATCC) that were cultured in the Freestyle 293 expression medium (GIBCO) at 37°C and 5% CO<sub>2</sub>. Baculovirus for infecting HEK293S GnTI<sup>-</sup> cells was produced in Sf9 cells (GIBCO) that were cultured in the Sf-900 III SFM media (GIBCO) at 27°C. S1S2 protein expression was performed in Escherichia coli Origami B (DE3) cells (Novagen). Cells were cultured in LB media at 37°C until OD<sub>600</sub> reached the value of 1.0-1.2, then cooled down to 20°C, induced with 250 μM IPTG and incubated for another 20 hours at 20°C. COS-7 cells for calcium imaging experiments were maintained at 37°C and 5% CO2 in Dulbecco's Modified Eagle's Medium, supplemented with 5% fetal bovine serum and 1% penicillin/streptomycin.

### **METHOD DETAILS**

### Constructs

The full-length Arabidopsis thaliana GLR3.4 (residues 1-959; Uniprot Q8GXJ4, NCBI NP\_001030971.1) was introduced into a pEG BacMam vector for baculovirus-based protein expression in mammalian cells (Goehring et al., 2014), with the C-terminal thrombin cleavage site (LVPRGS), followed by eGFP and streptavidin affinity tag (WSHPQFEK). The GLR3.4-S1S2 construct for expression of the isolated LBD was made by introducing S1 (residues 492-601) and S2 (residues 709-842) fragments of GLR3.4 connected by the glycine-threonine (GT) linker into a pET22b vector (Novagen), with the N-terminal 8xHis affinity tag followed by the thrombin cleavage site. The boundaries of S1 and S2 were determined based on sequence alignment of GLR3.4 with GluA2 and GLR3.2 LBDs (Armstrong and Gouaux, 2000; Armstrong et al., 1998; Sobolevsky et al., 2009).

For expression in COS-7 cells, full-length GLR3.4 cDNA was amplified by PCR from vector pDS\_EF1-XB-glr3.4-CFP (from Spalding's lab) with the primer pair B579/B580. The resulting PCR product was cloned into Notl/Xhol digested pcDNA3 via GIA (Gibson Isothermal Assembly) to yield pcDNA3-atglr3.4. In order to generate the mutant pcDNA3-atglr3.4(C205A), two PCRs were performed using pcDNA3-atglr3.4 as template with the primer pairs B579/C328 and C329/B580. The resulting PCR products were cloned into Notl/Xhol digested pcDNA3 via GIA.

For expression in Arabidopsis pollen, a custom gateway destination vector, pGreenII-OLE1p::OLE1::eGFP atUBQ10p::Gateway::eGFP, was generated. The pLat52 Gateway cassette with C-terminal eGFP was PCR amplified with the primer pair B193/B204



Molecular Cell Article

using pK7FWG2-Lat52 (Wudick et al., 2018b) as a template and the resulting product was digested with Spel and purified. PCR using *Arabidopsis* Col-0 gDNA was performed with the primer pair B278/B279 to amplify the atUBQ10 (At4g05320) promoter. Both PCR products were then cloned into Kpnl/EcoRl digested pGreenIl-OLE1p::OLE1::eGFP Lat52p::Gateway (Wudick et al., 2018b) via GIA. The genomic coding sequence of atglr3.4 was amplified with primer pair B394/B395 via PCR using *Arabidiopsis* Col-0 gDNA as a template. The resulting PCR product was then used in a Gateway BP reaction with pDONR201 to create the donor clone, pDONR201-atglr3.4. A Gateway LR reaction was performed with donor clone pDONR201-atglr3.4(gDNA) and destination clone pGreenII-OLE1-p::OLE1::eGFP atUBQ10p::Gateway::eGFP to generate the expression clone pGreenII-OLE1p::OLE1::eGFP atUBQ10p::atglr3.4 (gDNA)::eGFP.

#### **Plant transformation**

Expression construct pGreenII-OLE1p::OLE1::eGFP atUBQ10p::atglr3.4(gDNA)::eGFP was transformed into Agrobacteria strain GV3101 harboring the pSoup helper plasmid via electroporation. *Arabidopsis thaliana* Col-0 plants were then transformed via the floral dip method according to standard protocols (Wudick et al., 2018b).

### GLR3.4-S1S2 expression and purification

GLR3.4-S1S2 was transformed into *Escherichia coli* Origami B (DE3) cells and grown in LB media supplemented with 100  $\mu$ g/ml ampicillin, 15  $\mu$ g/ml kanamycin and 12.5  $\mu$ g/ml tetracycline. The freshly inoculated culture was grown at 37°C until OD<sub>600</sub> reached the value of 0.8-1.2. Then cells were cooled down to 20°C, induced with 250  $\mu$ M isopropyl  $\beta$ -d-1-thiogalactopyranoside (IPTG) and incubated in the orbital shaker for 20 hours at 20°C. The cells were harvested by centrifugation at 5,000 rpm for 15 min at 4°C and washed with the buffer containing 150 mM NaCl and 20 mM Tris pH 8.0.

For GLR3.4-S1S2<sub>GIU</sub>, all buffers in the following purification steps were supplemented with 1 mM L-glutamate. First, the cells were resuspended in the lysis buffer containing 200 mM NaCl, 20 mM Tris pH 7.5, 1 mM  $\beta$ -mercaptoethanol ( $\beta$ ME), 1 mM phenylmethy-sulfonyl fluoride (PMSF), 200  $\mu$ g/ml lysozyme, 5% glycerol and DNase and disrupted by sonication. After the lysate was centrifuged at 40,000 rpm using the Ti45 rotor for 1 hour at 4°C, the supernatant was mixed with His60 Ni superflow resin (Takara) and rotated for 2 hours at 4°C. The protein-bound resin was washed with the buffer containing 200 mM NaCl, 20 mM Tris pH 7.5, 1 mM  $\beta$ ME and 20 mM imidazole and the protein was eluted using the same buffer but containing 200 mM instead of 20 mM imidazole. The protein was 3x diluted in the buffer containing 150 mM NaCl, 20 mM Tris pH 7.5, 1 mM  $\beta$ ME and 5% glycerol and subjected to thrombin digestion (1:500 w/w) for 1.5 hour at 22°C. The protein was further purified using ion-exchange Hi-Trap Sepharose-SP (GE Healthcare).

For GLR3.4-S1S2<sub>Met</sub> and GLR3.4-S1S2<sub>Ser</sub>, protein purification was similar, except 1 mM L-glutamate was omitted from all purification buffers. In addition, instead of ion exchange chromatography, we used size-exclusion chromatography with the Superdex 16/60 column (GE Healthcare) and the buffer containing 150 mM NaCl, 20 mM Tris pH 7.5, 1 mM  $\beta$ ME, and 5% glycerol. The purified protein was evaluated using SDS-PAGE and FSEC (Superose 10/30 column, GE Healthcare) and supplemented with the corresponding ligand (Met) before subjecting it to crystallization.

### **GLR3.4-S1S2** crystallization and structure determination

Purified GLR3.4-S1S2<sub>Glu</sub> protein concentrated to  $\sim$ 8-10 mg/ml was first subjected to crystallization screening using Mosquito robot (TTP Labtech) in sitting drop vapor diffusion 96-well crystallization plates at 4°C. After two weeks, small octagonal crystals appeared in the condition consisting of 2 M ammonium sulfate and 0.1 M Sodium Acetate pH 4.6. For GLR3.4-S1S2<sub>Met</sub>, 1 mM methionine was added to the purified protein and the ligand-protein mixture was incubated for 30-40 min on ice before crystallization screening with Mosquito. By not adding any ligands to the protein we intended to solve the S1S2 structure in the apo state, but instead ended up solving the GLR3.4-S1S2<sub>Ser</sub> structure with serine of an apparent endogenous origin. Small octagon-shaped crystals of GLR3.4-S1S2<sub>Met</sub> and GLR3.4-S1S2<sub>Ser</sub> grew in 2 M ammonium sulfate at 4°C. All crystals were cryoprotected using crystal growth buffers supplemented with 25% glycerol and flash-frozen in liquid nitrogen. Crystal diffraction data were collected at the beamline 24-ID-C of the Advanced Photon Source (APS) and processed using XDS (Kabsch, 2010) and Aimless as a part of the CCP4 suite (Winn et al., 2011).

The structure of GLR3.4-S1S2<sub>Glu</sub> was solved by molecular replacement using Phaser (McCoy, 2007) and GLR3.2-S1S2<sub>Gly</sub> (PDB 6VEA) as a search probe. The model was refined by alternating cycles of building in COOT (Emsley and Cowtan, 2004) and automatic refinement in Phenix or Refmac (Adams et al., 2010). The structures of GLR3.4-S1S2<sub>Met</sub> and GLR3.4-S1S2<sub>Ser</sub> were solved by molecular replacement using the GLR3.4-S1S2<sub>Glu</sub> structure as a search probe. Water molecules were added manually in Coot. Analysis of possible inclusion of metal ions in the S1S2 crystal structures was performed using the CheckMyMetal validation tool (https://cmm.minorlab.org/) (Zheng et al., 2017a). All structural figures were prepared in Pymol (DeLano, 2002).

#### Measurements of ligand binding to GLR3.4-S1S2 using microscale thermophoresis

GLR3.4-S1S2 was purified as described above, except the N-terminal 8xHis tag was not cleaved by thrombin and remained with the protein. The unlabeled GLR3.4-S1S2 protein was subjected to microscale thermophoresis (MST) in the Monolith NT Label free (Nano Temper Technologies), which detected its intrinsic tryptophan fluorescence. The 1.5-μM purified protein stock solution was made using the interaction buffer containing 150 mM NaCl and 20 mM Tris pH 7.5. The stock solutions of the ligands L-glutamate,

### **Molecular Cell**

**Article** 



L-methionine, and L-serine were prepared at the concentration of 16 mM and serially diluted using the same buffer. For interaction measurements, the protein and ligand solutions were mixed at the 1:1 (v/v) ratio, with the protein concentration kept constant and the ligand concentration varied. The interaction mix was incubated at room temperature for 5-10 min and subjected to thermophoresis measurements in 16 capillaries with medium MST and 20% LED power at 24°C. For each ligand, the experiment was repeated 3-4 times and the data was averaged, normalized and fitted with the logistic equation using Origin 2015 software (OriginLab Corporation).

### Full-length GLR3.4 expression and purification

The GLR3.4 bacmid and baculovirus were made by using the standard methods (Goehring et al., 2014). The P2 virus was produced in Sf9 cells (GIBCO, 12659017) and added to HEK293S GnTI<sup>-</sup> cells (ATCC, CRL-3022) incubated at 37°C and 5% CO<sub>2</sub>. Cells were supplemented with 10 mM sodium butyrate 12 hours post infection and the temperature was changed to 30°C. Cell were harvested 72 hours post infection using low-speed centrifugation (5,500 g, 10 min), washed using 1X PBS pH 8.0 and pelleted again (5,500 g, 15 min). The pellet was resuspended in 50 mL per 1 L of the initial cell culture lysis buffer consisting of 150 mM NaCl, 20 mM Tris pH 8.0, 1 mM βME, 0.8 μM aprotinin, 2 μg/ml leupeptin, 2 μM pepstatin A and 1 mM PMSF and lysed by sonication. The lysate was centrifuged (9,900 g, 15 min) to remove cell debris and the supernatant was subjected to ultracentrifugation (186,000 g, 40 min) to pellet cell membranes. The membranes were mechanically homogenized and solubilized for 2 hours in the buffer containing 150 mM NaCl, 20 mM Tris-HCl pH 8.0, 1 mM βME and 1% digitonin (Cayman Chemical Company, 14952). Insoluble material was removed by ultracentrifugation (186,000 g, 40 min), while the supernatant was added to the pre-equilibrated Streptavidin-linked resin (2 mL resin per 1L of the initial cell culture) and the mixture was rotated for 10-14 hours at 4°C. The protein-bound resin was washed with 25 mL of the buffer containing 150 mM NaCl, 20 mM Tris-HCl pH 8.0 and 0.05% digitonin and the protein was eluted using the same buffer supplemented with 2.5 mM D-desthiobiotin. The eluted protein was subjected to thrombin digestion (1:300 w/w) at 22°C for 1 hour. The digest reaction was injected into Superose 6 10/30 size-exclusion column (GE Healthcare) equilibrated with the buffer containing 150 mM NaCl, 20 mM Tris-HCl pH 8.0, and 0.05% digitonin. The tetrameric GLR3.4 peak fractions were pooled, concentrated to ~2.5 mg/ml and used for cryo-EM sample preparation. All the steps, unless otherwise noted, were performed at 4°C.

#### **Cryo-EM sample preparation and data collection**

Au/Au grids were prepared as described in the literature (Russo and Passmore, 2014). Briefly, grids were prepared by first coating C-flat (Protochips, Inc., Morrisville, NC) CF-1.2/1.3-2Au 200 mesh holey carbon grids with ~50 nm of gold using an Edward Auto 306 evaporator. Subsequently, an Ar/O<sub>2</sub> plasma treatment (6 minutes, 50 W, 35.0 sccm Ar, 11.5 sccm O<sub>2</sub>) was used to remove the carbon with a Gatan Solarus (model 950) Advanced Plasma Cleaning System. The grids were again plasma treated (H<sub>2</sub>/O<sub>2</sub>, 20 s, 10 W, 6.4 sccm H<sub>2</sub>, 27.5 sccm O<sub>2</sub>) prior to sample application in order to make their surfaces hydrophilic. Purified GLR3.4 protein was mixed with 1 mM L-Glutamate and incubated on ice for  $\sim$ 30 min before grid preparation. A Vitrobot Mark IV (FEI) was used to plunge-freeze the grids after the application of 3 µl protein solution with 100% humidity at 4°C, a blot time of 3 s, blot force set to 3, and a wait time of 20 s. The grids were clipped and loaded into a 300 kV Titan Krios microscope equipped with Gatan K3 direct electron detection camera. 11,854 micrographs were collected in counting mode with a pixel size of  $0.83 \, \text{Å}$  ( $\sim 105,000 \, \text{x}$  magnification) across a defocus range of  $-1.0 \, \mu \text{m}$  to  $-2 \, \mu \text{m}$ . The total dose of 58 e<sup>-</sup>Å<sup>-2</sup> was attained by using a dose rate of  $\sim$ 16.0 e<sup>-</sup>pixel<sup>-1</sup>s<sup>-1</sup> across 50 frames for 2.5 s total exposure time.

### Image processing

The total of 11,854 micrographs were collected as two datasets, dataset 1 (6,119 micrographs) and dataset 2 (5,735 micrographs) and initially processed in Relion 3.1 (Zivanov et al., 2018). Frame alignment was done using MotionCor2 (Zheng et al., 2017b). CTF estimation was performed using Gctf (Zhang, 2016) on non-dose-weighted micrographs while subsequent data processing was done on dose-weighted micrographs. For each dataset, ~3,000 particles were manually selected to generate 2D classes that were used as templates to autopick 1,044,465 particles from dataset 1 and 1,116,729 particles from dataset 2. The particle images were 4x4 binned to a pixel size of 3.32 Å/pixel and subjected to 3D classification, each dataset into ten classes. A density map was generated in Chimera from the crystal structure of GluA2 (PDB ID: 3KG2), low-pass filtered to 40 Å, and used as an initial reference. The best 3D classes contained 190,076 particles for dataset 1 and 145,948 particles for dataset 2, which were further unbinned to a pixel size of 0.83 Å/pixel and re-extracted. These particles were cleaned up by 3D classification and subsequently subjected to Bayesian polishing and CTF refinement. After refinement and postprocessing, the resulting 109,759 particles for dataset 1 and 117,856 particles for dataset 2 produced 3D maps at the resolution of 5.0 and 4.2 Å, respectively. Then the particles for datasets 1 and 2 were joined and subjected to micelle subtraction and multiple rounds of 3D classification to reduce particle heterogeneity. After additional beam tilt CTF refinement, followed by regular refinement and postprocessing, the remaining 118,592 cleaned up particles produced a map at the resolution of 3.73 Å. These particles were imported into cryoSPARC (Punjani et al., 2017) and subjected to several rounds of 2D clean up, homogeneous and non-uniform refinement with C2 symmetry, resulting in a final map at 3.57 Å resolution (110,630 particles). Focused classification and focused refinement were performed to improve density in the TMD region (Figure S3D). The total of 227,615 combined particles from the two datasets were particle subtracted in Relion 3.1 by providing a soft mask around the LBD-TMD region. The subtracted particles were refined, cleaned by several rounds of 2D classification in Relion 3.1 and refined again with a soft mask to yield a final map at 4.39 Å resolution (174,044 particles). The overall resolution was estimated using the Fourier shell correlation (FSC = 0.143) criterion on masking-effect-corrected FSC curves calculated between two independent half-maps



**Molecular Cell** 

(Chen et al., 2013; Scheres, 2012). The local resolutions were estimated with unfiltered half-maps using ResMap (Kucukelbir et al., 2014) and EM density maps were visualized using UCSF Chimera (Pettersen et al., 2004).

#### **Model building**

For model building of the LBD, the GLR3.4-S1S2<sub>Glu</sub> crystal structure was used as a guide. To guide model building of the ATD and TMD, homology models of these domains were created using Swiss-Model (Waterhouse et al., 2018) and the GluA2 structure (PDB ID: 3KG2) as a template. The remaining parts of GLR3.4 were built de novo using cryo-EM density as a guide. The resulting model was real space refined in Phenix (Afonine et al., 2012) and visualized using Chimera (Pettersen et al., 2004) or Pymol (DeLano, 2002). The analysis of intersubunit interfaces as well as surface area calculations were performed using the PDBePISA web service (https:// www.ebi.ac.uk/pdbe/prot\_int/pistart.html) (Krissinel and Henrick, 2007).

#### **Cysteine crosslinking**

Cysteine substitutions were introduced using conventional PCR-based methods. Constructs were verified by sequencing over the entire length of the GLR3.4 coding region. Wild-type and cysteine-substituted GLR3.4 proteins were expressed and purified as described above, except 1% lauryl maltose neopentyl glycol (LMNG) detergent (Anatrace) was used instead of digitonin for protein extraction. Binding of protein to streptavidin-linked resin lasted for 1 hour. Instead of 0.05% of digitonin, 0.1 mM LMNG was in the buffers that were used to wash the protein-bound resin, elute the protein, and for size-exclusion chromatography. For crosslinking,  $\sim$ 2.5  $\mu$ g of protein was subjected to denaturing conditions by addition of SDS sample buffer in the absence (non-reducing condition) or presence (reducing condition) of 600 mM dithiothreitol (DTT). The protein samples were then run on a 4%-15% gradient SDS-PAGE gel and protein bands were visualized by AguaStain Protein Gel Stain (Bulldog Bio). The oligomeric state of wild-type and cysteine-substituted GLR3.4 was assessed by subjecting  $\sim$ 2  $\mu$ g of protein to FSEC.

### COS-7 cells transfection and Ca2+ imaging

Protocols for COS-7 cells transfection and Ca<sup>2+</sup> imaging were adapted from the previous studies (Ortiz-Ramírez et al., 2017). COS-7 cells (Sigma-Aldrich) were maintained at 37°C and 5% CO<sub>2</sub> in Dulbecco's Modified Eagle's Medium, supplemented with 5% fetal bovine serum and 1% penicillin/streptomycin (GIBCO), and transfected at low passage (p < 7). Cells were plated at a density at 50% confluence in 35-mm diameter dishes and transfected using FugeneHD (Promega) as specified by the supplier. Cells were co-transfected with pCI-AtCNIH4 (0.2 μg), pCI-AtCNIH1 (0.2 μg), pcDNA3-AtGLR3.4 (0.8 μg) and pEF1-YC3.6 (0.5 μg). The co-transfection with pCI-AtCNIH4 and pCI-AtCNIH1 was previously shown to enhance functional expression and activity of GLRs (Wudick et al., 2018b). In experiments illustrated in Figure S2E, pCI-AtCNIH4 was increased to 0.4 µg (red circles) and replaced by empty pCI plasmid in cells expressing AtGLR3.4 alone (black circles). Cells were used for imaging 38 to 41 hours after transfection. They were washed in a Ca<sup>2+</sup>-free solution (1 mM EGTA, 10 mM Bis-Tris propane buffered to pH 7.3 with HEPES and set to 350 mOsmol with D-mannitol). Cells were imaged in the Ca<sup>2+</sup>-free solution for 1.5 min before the addition of Ca<sup>2+</sup> to a final concentration of 14.5 mM (using Ca-Gluconate). The ligands (Glu, Asn, or Gly; 0.5 or 1.0 mM) were added at the beginning, before Ca<sup>2+</sup> was introduced. L-glutamate, Glycine and L-Asparagine were prepared as 100 mM stock solutions (Sigma-Aldrich, St. Louis, MO, USA). L-Glu stock solution was adjusted to pH 7.0 with Bis-tris propane. Timelapse acquisition was performed with a sampling interval of 30 s. 8 to 12 cells were imaged in each dish using the stage position recording tool of the microscope system. Imaging was performed at room temperature using a DeltaVision Elite Deconvolution/TIRF microscope system (Olympus inverted IX-71) under a 60X lens (1.2NA UPLSAPO water /WD 0.28 mm). A xenon lamp from the DeltaVision system was used with a CFP excitation filter (438-424 nm). Two simultaneous emission records were captured: YFP emission (548-522 nm) and CFP emission (475-424 nm). To minimize bleaching, the laser was set to 2%. YFP and CFP imaging were recorded with 0.6 s exposure time. Images were processed using ImageJ. Ratios were obtained after background subtraction and signal clipping using the "Ratioplus" plug-in for ImageJ. The signal of each channel was averaged in a circle in the middle of the cell (with 100-200 pixel diameter, depending on the size of the cell). The YFP/CFP ratio was obtained by dividing the emission recorded for YFP (548-522 nm) by the one recorded for CFP (475-424 nm). No significant bleaching or ratio drift was observed in our experimental conditions.

### **Patch-clamp recordings**

For patch-clamp recordings, COS-7 cells were maintained and transfected according to the protocol described in the COS-7 cells transfection and Ca<sup>2+</sup> imaging section. Cells were co-transfected with pCI-AtCNIH4 (0.2 μg), pCI-AtCNIH1 (0.2 μg), pcDNA3-AtGLR3.4 (0.4 μg) and pIRES-CD8 (0.05 μg), the latter to select transfected cells with the help of anti-CD8 antibody-coated beads (Dynabeads, Thermo Fisher Scientific, USA). In experiments described in Figure S2B, the quantity of pcDNA3-AtGLR3.4 was increased to 0.8 µg. Patch-clamp was performed in the whole-cell configuration, 39 to 45 hours after transfection. Pipettes were pulled using a P97 puller (Sutter Instrument, Novato, CA, USA). Their resistance was 3-5 M $\Omega$  in the bath solution. Whole-cell currents were recorded at the sampling frequency of 2-4 kHz and filtered at 1-2 kHz using an Axopatch 200A amplifier with an Axon 1200 DigiData analog-to-digital converter and pCLAMP software (Molecular Devices, Sunnyvale, CA, USA). The pipette solution contained 150 mM Na-Gluconate, 3 mM MgCl<sub>2</sub>, 4 mM HCl, 5 mM EGTA, and 10 mM Bis-tris-propane pH 7.2 (adjusted using HEPES). The bath solution contained 20 mM Ca-Gluconate, 10 mM Na-Gluconate and 10 mM Bis-tris propane pH 6.5 (adjusted using MES). Solutions were adjusted to 350 mOsmol with D-mannitol. L-glutamate, Glycine and L-Asparagine were prepared as 100 mM stock solutions (Sigma-Aldrich, St. Louis, MO, USA). L-Glu stock solution was adjusted to pH 7.0 with Bis-tris propane. In experiments illustrated in

### **Molecular Cell**

**Article** 



Figure S2C, washout was performed by gravity perfusion at the rate of 1 mL per minute. For the experiments with GSH, the pipette solution contained: 150 mM NaCl, 3 mM MgCl<sub>2</sub>, 10 mM BTP, 5 mM EGTA, and 100 nM free Ca<sup>2+</sup>. pH was adjusted to 7.3 with HEPES and osmolarity to 350 mOsmol with D-mannitol. Bathing solution contained: 15 mM CaCl<sub>2</sub> and 10 mM BTP. pH was adjusted to 7.3 with HEPES and osmolarity to 350 mOsmol with D-mannitol. The voltage protocol during current acquisition followed the sequence: (1) cells were clamped at a holding potential of 0 mV, and (2) 1.5-s voltage pulses were applied in the range of -100 to +60 mV with the 20-mV steps. The holding potential was returned to 0 mV for 1.1 s between the pulses.

#### **Extracellular calcium influx measurements**

Extracellular Ca<sup>2+</sup> influx was measured at the tip of the pollen tubes using the ion-selective vibrating probe with simultaneous growth rate monitoring, as described previously (Wudick et al., 2018b). Measurements were performed in two Arabidopsis thaliana independent T-DNA insertion lines, Atglr3.4-1 (SALK\_201768) and Atglr3.4-2 (SALK\_079842), while Col-0 was used as wild-type. Plants were grown under short-day conditions (12 hours of light at 22°C and 12 hours of dark at 18°C, with an irradiance of ca. 100 μmol m<sup>-2</sup>sec<sup>-1</sup>). Arabidopsis pollen grains were collected from fresh flowers and then germinated in liquid medium containing 500 μM KCI, 500 μΜ CaCl<sub>2</sub>, 125 μM MgSO<sub>4</sub>, 0.005% H<sub>3</sub>BO<sub>3</sub>, 125 μM HEPES pH 7.5 and 16% sucrose. Pollen grains were incubated at 21.5°C for at least 3 hours. Growing pollen tubes longer than 150 µm were selected for flux and growth rate measurements.

### Confocal microscopy of Arabidopsis pollen

Wild-type Col-0 pollen stably expressing UBQ10:GLR3.4-GFP was mounted in germination medium (500 μM KCI, 500 μM CaCl<sub>2</sub>, 125 μM MgSO<sub>4</sub>, 0.005% H<sub>3</sub>BO<sub>3</sub>, 125 μM HEPES pH 7.5 and 16% sucrose) and visualized using the 63 × /1.4 plan- apochromat objective of a Zeiss LSM700 laser scanning confocal microscope using the 488 nm laser for excitation (emission recorded at 500-530 nm). Image analysis was performed using ImageJ (https://rsbweb.nih.gov/ij/).

### Liquid chromatography and mass spectrometry

Purified full-length GLR3.4 was alkylated with 40 mM 2-chloroacetamide (CAA, Sigma-Aldrich) followed by the addition of Urea (Sigma-Aldrich) to a final concentration of 8 M. For reducing conditions, tris(2-carboxyethyl)phosphine hydrochloride (TCEP, Sigma-Aldrich) was added to a final concentration of 10 mM. The resulting solution was heated to 37°C for 1 h. Next, the samples were diluted with 50 mM ammonium bicarbonate (Sigma-Aldrich) and digested by a combination of LysC (Wako) and Trypsin (Promega). The final peptide mixtures were acidified with formic acid (Sigma-Aldrich) to a final concentration of 1% and then desalted with CDS Empore<sup>TM</sup> SDB-RPS (Fischer Scientific) in house-packed stage-tips (Rappsilber et al., 2007).

Desalted peptides were injected into an EASY-Spray PepMap RSLC C18 50 cm x 75 µm column (Thermo Scientific), which was coupled to the Orbitrap Fusion Tribrid mass spectrometer (Thermo Scientific). Peptides were eluted at the flow rate of 250 nL/min with a non-linear 120-min gradient of 5%-30% buffer B consisted of 0.1% (v/v) formic acid and 100% acetonitrile. The column temperature was maintained at 50°C throughout the entire experiment. Thermo Scientific Orbitrap Fusion Tribrid mass spectrometer was used for peptide MS/MS analysis. Survey scans of peptide precursors were performed from 350 to 1500 m/z at 120K FWHM resolution (at 200 m/z) with a 2 × 105 ion count target and a maximum injection time of 60 ms. The instrument was set to run in top speed mode with 3 s cycles for the survey and the MS/MS scans. After the survey scan, tandem MS was performed on the most abundant precursors exhibiting a charge state from 2 to 6 of greater than 2 x 105 intensity by isolating them in the quadrupole at 1.6 Th. HCD fragmentation was applied with 30% collision energy and the resulting fragments were detected using the auto: m/z Normal in the Orbitrap. The AGC target for MS/MS was set to  $5 \times 10^4$  and the maximum injection time limited to 30 ms. The dynamic exclusion was set to 30 s with a 10 ppm mass tolerance around the precursor and its isotopes. Monoisotopic precursor selection was enabled.

The acquired raw data were analyzed with pFind software platform (Chi et al., 2018) against reduced database based on the reviewed Arabidopsis thaliana proteins (16,268 entries, version 2021\_02, downloaded from UniProt) from which 1,000 random entries plus GLR3.4 were retained. Full-specific mode with TrypsinKR\_C and up to two missed cleavages were used. Precursor tolerance and Fragment tolerance were set to 20 ppm. Modification search was performed in an open mode with Carbamidomethyl (C), Glutathione (C), and Oxidation (M) set as dynamic modifications. In case of Glutathione, a neutral loss was defined as 129.1148 Da. The FDR was set as 1% with the peptides mass in the range of 600-10,000 Da and the length between 6 and 100 residues. The raw files and full output tables are available through PRIDE repository with identifier PXD024563 (reviewer access username: reviewer\_pxd024563@ebi.ac.uk, password: UDehuNMe).

### **QUANTIFICATION AND STATISTICAL ANALYSIS**

Calcium imaging and confocal microscopy data (Figures 1B, S1, S2E, and S2F) were analyzed using ImageJ. Mass spectrometry data (Figure 3B) was analyzed using pFind. Statistical analysis was performed using SigmaPlot 11.0 (Figures 1A, 1B, 3C-3E, S1D, and S2) and Origin 2015 Sr2 (Figure S6E). In all figure legends, n represents the number of independent biological replicates. All quantitative data were presented as mean ± SEM. Statistical analyses were conducted using one-way ANOVA followed by the post hoc Dunnett test (Figures S1D and S2D). Values of p < 0.05 were considered statistically significant.